DISSERTATIONES
CHIMICAE
UNIVERSITATIS
TARTUENSIS
209

RIINU HÄRMAS

The structure and H_2 diffusion in porous carbide-derived carbon particles

DISSERTATIONES CHIMICAE UNIVERSITATIS TARTUENSIS
209

DISSERTATIONES CHIMICAE UNIVERSITATIS TARTUENSIS
209

RIINU HÄRMAS

The structure and H_2 diffusion in porous carbide-derived carbon particles

UNIVERSITY OF TARTU
Press
1632

Institute of Chemistry, Faculty of Science and Technology, University of Tartu, Estonia

The dissertation is accepted for the commencement of the degree of Doctor of Philosophy in Chemistry on January 27th, 2022, by the Council of Institute of Chemistry, University of Tartu.

Supervisors: Research Fellow Rasmus Palm, Ph.D.
University of Tartu, Estonia

Professor Enn Lust, Ph.D.
University of Tartu, Estonia

Opponent: Prof. Dr.-Ing. Bastian J.M. Etzold
Technische Universität Darmstadt

Commencement: 15.03.2022 at 12:15. Auditorium 1020, Ravila 14a, Tartu

European Union
European Regional
Development Fund

Investing
in your future

ISSN 1406-0299
ISBN 978-9949-03-831-2 (print)
ISBN 978-9949-03-832-9 (pdf)

University of Tartu Press
www.tyk.ee

TABLE OF CONTENTS

1. LIST OF ORIGINAL PUBLICATIONS

I. E. Härk, A. Petzold, G. Goerigk, S. Risse, I. Tallo, **R. Härmas**, E. Lust, M. Ballauff, Carbide Derived Carbons Investigated by Small-Angle X-Ray Scattering: Inner Surface and Porosity vs. Graphitization, Carbon. 146 (2019), 284–292.

II. R. Palm, **R. Härmas**, E. Härk, B. Kent, H. Kurig, M. Koppel, M. Russina, I. Tallo, T. Romann, J. Mata, K. Tuul, E. Lust, Study of the structural curvature in Mo_2C derived carbons with contrast matched small-angle neutron scattering, Carbon. 171 (2021), 695−703.

III. **R. Härmas**, R. Palm, H. Kurig, L. Puusepp, T. Pfaff, T. Romann, J. Aruväli, I. Tallo, T. Thomberg, A. Jänes, E. Lust, Carbide-Derived Carbons: WAXS and Raman Spectra for Detailed Structural Analysis, C. 7 (2021), 29.

IV. **R. Härmas**, R. Palm, M. Russina, H. Kurig, V. Grzimek, E. Härk, M. Koppel, I. Tallo, M. Paalo, O. Oll, J. Embs, E. Lust, Transport Properties of H_2 Confined in Carbide-Derived Carbons with Different Pore Shapes and Sizes. Carbon. 155 (2019), 122–128.

Author's contribution:

Paper I: Measured gas adsorption data and performed the analysis of gas adsorption data.

Paper II: Participated in the experiment and in the preparation of the manuscript.

Paper III: Performed data analysis (all except the fitting of the WAXS data) and was mainly responsible for the preparation of the manuscript.

Paper IV: Performed the analysis QENS data of SiC and Mo_2C derived carbons and participated in the preparation and publication of the manuscript.

2. ACRONYMS AND SYMBOLS

$\langle N \rangle$	the average number of layers in a stack
2D-NLDFT	two-dimensional non-local-density functional theory
a_3	average interlayer spacing
$A_{\Sigma D}/A_{\Sigma G}$	ratio, where the sum of the areas of the D_S band and D band is divided by the sum of the areas of the G_S and the G band
B_{fl}	the scattering contribution of the carbon phase, which becomes dominant at large q values
CDC	carbide-derived carbon
CLD	chord length distribution
D'	band in the Raman spectrum characteristic of sp^2 carbon at 1620 cm^{-1}
D or D_A	band in the Raman spectrum characteristic of sp^2 carbon at ~1350 cm^{-1}
D_0	the maximal diffusion coefficient
DFT	density functional theory
D_S	band in the Raman spectrum characteristic of sp^2 carbon at ~1200 cm^{-1}
D_T	(temperature dependent) diffusion coefficient
$d\Sigma/d\Omega(q)$	macroscopic differential scattering cross section of the sample
$d\Sigma_{fluct}/d\Omega(q)$	macroscopic differential scattering cross section of the density fluctuations and inaccessible pores in the sample
$d\Sigma_m/d\Omega(q)$	macroscopic differential scattering cross section normalized by sample mass
$d\Sigma_{pores}/d\Omega(q)$	macroscopic differential scattering cross section representing the scattering between the open pores and the carbon matrix
E_a	activation energy (of self-diffusion)
E_{laser}	energy of laser beam
FWHM	full width at half maximum
G or G_A	band in the Raman spectrum characteristic of sp^2 carbon at ~1580–1600 cm^{-1}
$g(r)$	chord length distribution
G_S	band in the Raman spectrum of sp^2 carbon at 1550 cm^{-1}
HR-SEM	high-resolution scanning electron microscopy
HTC	hydrothermal carbonization
I_D/I_G	ratio of the intensities (as band heights) of the D and the G band
IUPAC	International Union of Pure and Applied Chemistry
L_a	average graphene layer extent
L_c	average stacking size (of graphene layers)
l_{cc}	average C-C bond length
l_p^{SAXS}	number-averaged chord-length
l_R	Ruland length, describes the size above which the lateral correlation in the graphene layer is lost

n_{H2}	the amount of H_2 in the sample cell normalized by the mass of the carbon sample
NLDFT	non-local density functional theory
p	pressure
$p/p°$	relative pressure
$p°$	saturation pressure
p_{H2}	pressure of hydrogen
$p_{H2,load}$	equilibrium pressure of H_2 in the sample holder at 77 K
q	scattering vector defined as $q = (4\pi/\lambda)\sin\theta$, where the 2θ is the scattering angle
QENS	quasi-elastic neutron scattering
QSDFT	quenched solid density functional theory
R^2	coefficient of determination
R_g	radius of gyration (generalized Guinier-Porod model)
s	dimensionality parameter (generalized Guinier-Porod model)
S/m	inner surface area
SANS	small-angle neutron scattering method
SAS	small-angle scattering
SAXS	small-angle X-ray scattering method
S_{DFT}	specific surface area calculated with 2D-NLDFT model
$S_{exp}(q, \Delta E)$	experimentally measured dynamic structure factor
$S_{inc}(q, \Delta E)$	incoherent dynamic structure factor
SLD	scattering length density
T	temperature
TEM	transmission electron microscopy
T_{syn}	synthesis temperature of carbide-derived carbon
w	pore width
WANS	wide-angle neutron scattering method
WAXS	wide-angle X-ray scattering method
V_{tot}	total volume of pores calculated from the amount of adsorbed gas near the saturation pressure, $p/p° = 0.95$
Γ_D	full width at half maximum of the D band of carbon
Γ_G	full width at half maximum of the G band of carbon
Γ_{QE}	full width at half maximum of the quasi-elastic broadening
ΔE	energy transfer
θ	scattering angle
λ	wavelength
λ_L	laser wavelength
ρ_f	apparent filling density of carbon particles
σ_1	standard deviation of the first-neighbor distribution for sp^2 carbon
σ_3	standard deviation of interlayer spacing for sp^2 carbon

3. INTRODUCTION

Carbon as a chemical element is ubiquituous in the nature. Alongside hydrogen, oxygen and nitrogen, carbon can form innumerable amount of different compounds and materials. Even in the pure form, carbon constitutes non-identical cystalline materials like diamond, graphite and molecular materials like graphene, fullerenes, nanotubes etc. In addition to these well-defined, defect-free forms of pure carbon, there exists countless forms of more or less disordered carbon materials. The disordered forms of carbons can consist of mainly sp^3 or sp^2 hybridized carbon or of a mixture of them [1]. The disordered carbon which contains mostly sp^2 carbon conducts electricity, is typically soot-like in appearance and can be very porous. Porous sp^2 carbons are usually well known as activated carbons. The term *activation* denotes a chemical and/or physical process in which the specific surface area and pore volume of a carbon material are enhanced. Activated carbons are used widely in air- and water purification systems, electrode materials for electrochemical appliances and other more specific uses [2].

Not all porous sp^2 carbons have undergone activation. Namely, carbide derived carbons (CDCs) have high specific surface area and specific pore volume already after the synthesis and do not need further activation. While typical precursors to activated carbons are different organic substances (coconut shells, peat, leaves etc.), the precursor to CDCs are inorganic carbides. The structure of carbide-derived carbon is easily controlled by choosing different precursor carbide and synthesis conditions. The resulting CDCs have the coveted benefit of a well-defined and narrow pore size distribution and are often very pure and free of additives [3].

Throughout the years CDCs have been successfully used in multiple applications, like supercapacitors [4], polymer-electrolyte fuel cells [5], batteries [6,7] and in gas adsorption applications [3]. In order to be able to explain in more detail the effect of the nanostructure of carbon material on the electrochemical and other (e.g H_2 adsorption) performance parameters, it is important to characterize the structure of the carbon thoroughly. This thesis aims to

- take a systematic look over a wide dataset of wide-angle X-ray scattering and Raman spectroscopy data of different CDCs to gain structural information,
- discern the change of the structure of Mo_2C-derived carbon with increasing temperature of synthesis using small-angle scattering methods,
- investigate the impact of the structure of CDCs to the H_2 diffusion characteristics in these carbons using quasi-elastic neutron scattering method.

4. LITERATURE OVERVIEW

4.1. Microporous carbons

Carbon has been used for purposes other than as a fuel or in metallurgy since ancient times. One of the oldest records can be seen in an Egyptian papyrus (1550 B.C.), where various carbons are mentioned for medicinal use [8]. Nowadays, porous carbons are used on a large scale in air and water purification applications, but an emerging important use for porous carbons lies in the electrochemical energy storage/conversion field. Namely, porous carbon materials are used as electrode materials in supercapacitors, batteries and polymer electrolyte membrane fuel cells.

A very important characteristic of a porous carbon is its average pore size and overall porous structure (i.e. pore-size distribution). Pores are classified according to their widths, w, as micropores ($w < 2$ nm), mesopores (2 nm $< w < 50$ nm) and macropores ($w > 50$ nm) (Figure 1a) [9]. The pore width is defined as the diameter in the case of cylindrical pores or as the distance between opposite walls in the case of slit-shaped pores. According to the definition of IUPAC (International Union of Pure and Applied Chemistry), microporous carbons are carbon materials, which are considered to have a major part of its porosity in micropores and exhibit apparent surface areas usually higher than 200 $m^2\ g^{-1}$ [10]. These small pores form in between the aromatic sheets and strips of sp^2 carbon, which are often bent and resemble a mixture of wood shavings and crumpled paper[1] (Figure 1b,c) [12]. The theoretical upper limit of surface area of activated carbon material is 2965 $m^2\ g^{-1}$, which corresponds to the specific surface area of an infinitely large double-sided graphene sheet) [13].

The relative orderliness of this disordered material can best be described by the size of the aromatic sheets or graphene-like platelets or domains of sp^2 carbon. These platelets are typically few nanometers wide and are not stacked in an orderly manner. When the carbon material is heated to >2000 °C, some of the platelets can join and, thus, the carbon material will become more ordered and the electrical and thermal conductivity of carbon material increases. Finally, if the heat-treatment temperature is high enough, the carbon can become competely graphitic, i.e. contain large graphene sheets, which are stacked in a crystalline manner (see section 4.2.3). This step-by-step increase in the graphitic order of disordered carbon material with the increase in the heat-treatment temperature is called the graphitization pathway (Figure 1d).

[1] For a thorough overview of different representations of the structure of disordered and amorphous carbons, reader is referenced to the review by P. J. F. Harris [11].

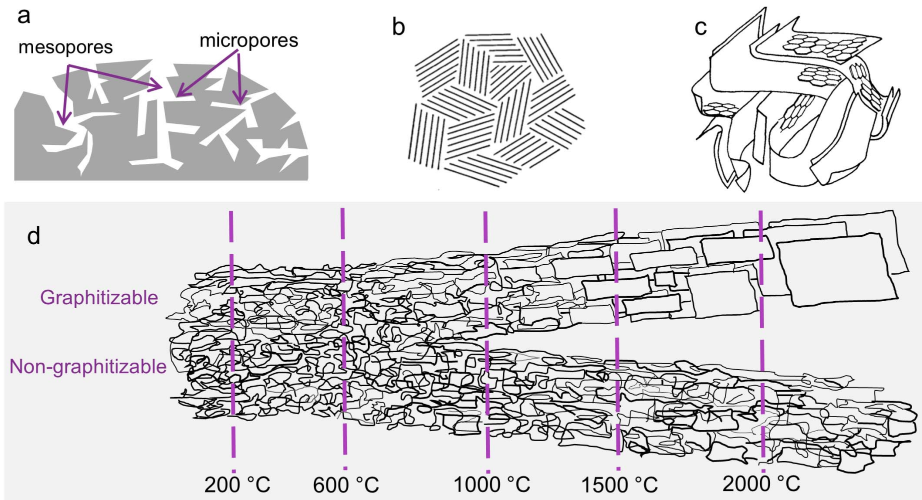

Figure 1. (a–c) Different representations of the structure of microporous carbon materials [12,14,15]. (d) Representation of the graphitization pathway for graphitizable and non-graphitizable, i.e. hard carbon [16].

R. E. Franklin coined the terms "graphitic" and "non-graphitic", to distinguish sp^2 carbons with a 3D ordered structure and 2D ordered structure, respectively. Namely, non-graphitic carbons contain graphene-like platelets with some degree of order, but these platelets are not stacked in an orderly manner, while 3D carbons contain well ordered stacks of graphene platelets [17].

4.1.1. Synthesis of microporous carbons

Various precursor materials and synthesis routes can be used to produce microporous carbon materials. The properties, e.g. average pore size, level of graphitization, etc. depend on both the precursor and the synthesis method applied. The synthesis of a porous carbon can consist of the following typical stages [3,8]:

1. the carbonization, i.e. the conversion of an organic substance into carbon or a carbon-containing residue,
2. the activation, i.e. process which enhances the specific surface area and pore volume,
3. the treatment with Ar, H_2 or N_2 at high temperature in order to clean the surface from unwanted functional groups.

The common method for carbonization is pyrolysis, i.e. the heat-treatment of some carbon-containing substance, often waste (e.g. corn stalks, fruit stones, coconut shells) in an inert atmosphere [18]. Another way to carbonize a carbon-containing precursor is to use hydrothermal carbonization (HTC). In HTC, the carbon-containing precursor is mixed with water and heated ($T > 100$ °C) in an enclosed autoclave, where the pressure can reach >0,1 MPa [19–21].

Activation can be done either using gas phase activation (so-called physical activation) or some solid/liquid reagents based (so-called chemical) activation. Activation can be achieved when the initial material is impregnated or mixed with an activating reagent (e.g. KOH, $ZnCl_2$) and then heated in inert atmosphere [18].

In a different approach entirely, carbide-derived carbons are derived from inorganic carbides usually via a chemical reaction at a high temperature. Although similar in terms of properties to the activated carbons, the CDCs can not be named "activated" since no activation is usually necessary to obtain a high specific surface area. The CDCs are mostly synthesized from metal or non-metal (Me) containing carbides (Me_xC) by halogenation, thermal or hydrothermal processing [3]. In the case of chlorination, the porous carbon material is formed when the Me atoms of the crystal structure of the carbide react with chlorine at the synthesis temperature, T_{syn}, and, thus, leave behind the carbon skeleton:

$$Me_xC(s) + xy/2\ Cl_2(g) \rightarrow x\ MeCl_y(g) + C(s). \quad (1)$$

The volatile product $MeCl_y$ is guided away in excessive Ar flow (collected and reused) and any remaining chlorine and/or functional groups are reduced in hydrogen gas flow at high temperature. Resulting carbons are noted as C-X Y in the text, where X denotes the precursor carbide and Y denotes the synthesis temperature in degrees of Celsius applied.

The higher the temperature of chlorination, the higher the level of graphitization of the formed CDC [22–24]. In comparison to traditional activated carbons, the CDCs contain little to no impurities and have a structure that can be easily controlled to range from very disordered to well-organized nano-graphitic. In addition, the pore size distribution of CDCs is typically narrower than the pore size distribution of typical activated carbons [3,22,23,25]. The CDCs have been used in electrochemical applications with excellent results, e.g. as the electrode materials for supercapacitors [4], as catalyst carriers for polymer-electrolyte membrane fuel cells (PEMFC) [5] and in other applications such as the gas (including H_2) adsorption [3].

4.2. Physical characterization methods of carbons

Gas adsorption analysis is the most common method to characterize the porous structure of various carbon materials. Different gases and measurement conditions are used, which give somewhat different information. Gas adsorption analysis characterizes the open porosity in the length scale of 0.4 nm to ~50 nm (Figure 2) [26,27]. Small-angle scattering methods (either X-ray, i.e. SAXS, or neutron, i.e. SANS) also give insight to the porous structure and, in addition to open porosity, give information about the possible closed porosity [28–31].

In order to gain insight about the relative disorder of the carbon (i.e. the average graphene domain length, average stacking height etc.), Raman spectroscopy and X-ray (or neutron) diffraction methods are used. However, the method known as X-Ray diffraction (XRD) is named Wide-Angle X-ray scattering (WAXS) henceforth, since the term "diffraction" should only be used when the studied materials show truly crystalline domains. Although the thorough analysis of Raman spectroscopy can result in a tentative assessment of the average graphene domain length, as a vibrational spectroscopy, this method can not be directly related with a specific length scale analysis. Rather, Raman spectroscopy can give information on the electronic states, the phonon energy dispersion and the electron-phonon interaction in sp^2 carbon systems [32].

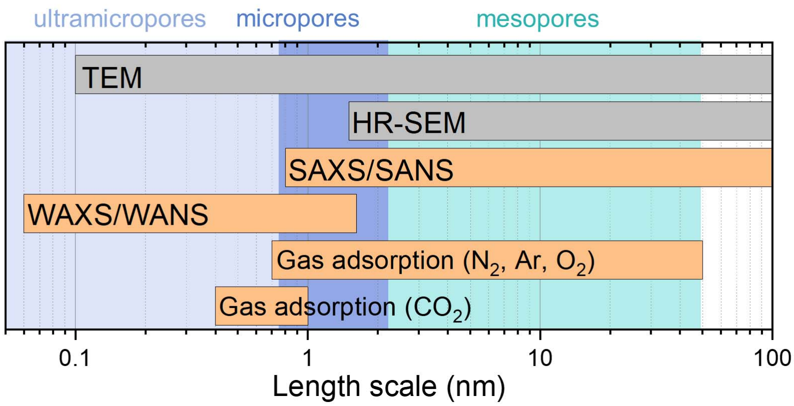

Figure 2. Length scales probed by different methods used for the characterization of porous carbon materials [27,33–35], orange color represents the methods used more thoroughly in this study, grey are the electron microscopy methods, which give unique, but not representative information about the sample structure.

4.2.1. Gas adsorption

Adsorption is a process by which the particles of one substance (atoms, molecules or ions) become attached to the external or internal surface (walls of capillaries, pores or crevices) of solids or the surface of liquids (Figure 3). The reverse process to adsorption is desorption.

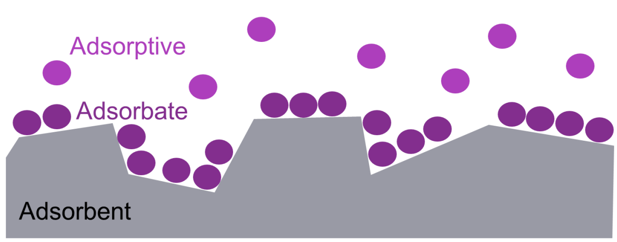

Figure 3. Schematic representation of the formation of a monolayer on an adsorbent.

In a gas adsorption analysis measurement the amount of adsorbed gas (i.e. adsorbate) in/on a solid (i.e. adsorbent) at increasing equilibrium pressure values of the adsorbate, p, at a constant temperature, T, (i.e. isothermal conditions) is obtained[2]. Thus, the adsorption curve is called an adsorption isotherm. When the p nearly reaches the saturation pressure of the adsorbate, $p°$, the pressure is gradually decreased and, thus, the desorption branch of the isotherm is measured. The obtained isotherm is characteristic of the porous structure (e.g. the specific surface area, the porosity and the pore dimensions) of the studied adsorbent. When describing the isotherm, the terms adsorption and desorption are used to indicate the direction from which experimentally determined amounts adsorbed have been approached – by reference to the adsorption curve (or point), or to the desorption curve (or point). When the adsorption and desorption curves do not coincide, so-called adsorption hysteresis arises. The experimentally observed adsorption isotherms can be classified according to IUPAC-recommendations to eight different types (Figure 4) [26].

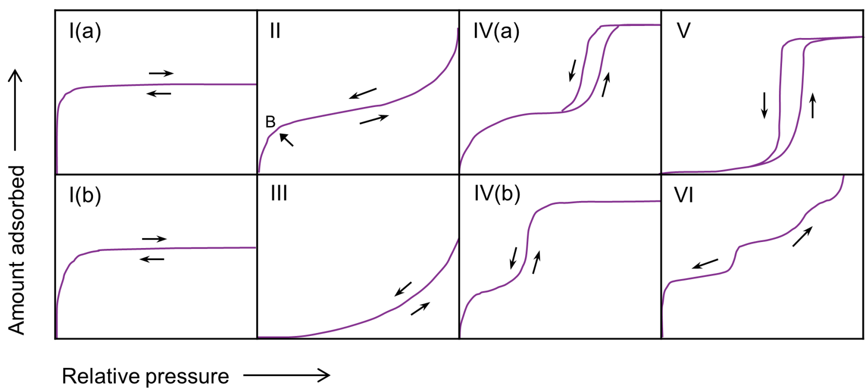

Figure 4. Classification of physisorption isotherms [26].

Type I isotherms are characteristic of microporous solids, while Type I(a) isotherms are given by materials having mainly narrow micropores (of width <1 nm) and Type I(b) isotherms are found for materials having pore size distributions over a broader range (< 2.5 nm). Type II isotherms are characteristic of the physisorption of gases on nonporous or macroporous adsorbents and the shape results from unrestricted monolayer-multilayer adsorption. Type III isotherm forms when the adsorbent-adsorbate interactions are weak and the adsorbed molecules are assembled near the most favorable sites on the surface of a nonporous or macroporous adsorbent. Type IV isotherms are typical to meso-

[2] More strictly, the quantity experimentally determined by gas adsorption is a surface excess amount, not the total amount adsorbed. However, when the pressure is low (<0.1 MPa), the surface excess amount and the total amount adsorbed can be considered equivalent [26].

porous adsorbents, while the capillary condensation is accompanied by hysteresis in Type IV(a), but no hysteresis in Type IV(b). The hysteresis occurs when the pore width exceeds a certain critical width, which is dependent on the adsorption system and temperature (e.g., for N_2 and Ar at 77 K and 87 K, respectively, hysteresis occurs for pores with $w > 4$ nm). When the mesopores in the adsorbent are of smaller width, completely reversible isotherms are seen (Type IVb). Type V occurs in the case of mesoporous materials, when the adsorbent–adsorbate interactions are weak. Type VI isotherms form when layer-by-layer adsorption occurs on a uniform nonporous surface [26].

The typical setting for gas adsorption/desorption measurement is to use nitrogen at pressures from 10^{-4} to 10^3 mbar at 77 K, i.e. at the boiling point of N_2 at atmospheric pressure. This setting in principle allows to characterize pores with widths in the range 0.7 to 50 nm (Table 1). However, the diffusion of N_2 at 77 K in the very narrow micropores is extremely slow. When materials containing these narrow micropores are measured with N_2 at $p/p° < 0.0001$, the equilibrium pressure may not be reached in a reasonable time or the measured points may not characterize the true adsorption equilibrium. The result of this is the underestimation of the experimental isotherm of N_2 in the low-pressure range [27].

The diffusion limitations of CO_2 are much smaller owing to the higher measurement temperature and the higher pressure at which micropore adsorption occurs in the case of CO_2 (Table 1). Thus, it is found that gas adsorption with CO_2 at 273 K is better suited to characterize the narrow micropores with widths between 0.4 and 1.0 nm [36]. In order to characterize the pore structure more accurately in a wide range of pore widths, it is recommended to measure both the N_2 and CO_2 isotherms and analyze the data in a global fitting of N_2 and CO_2 isotherms. Since the isotherm of CO_2 in the dual analysis provides the most accurate information about narrow micropores, the N_2 isotherm may be measured for the relative pressures starting at $p/p°$ about 0.001 rather than at 10^{-6} [27].

However, N_2 and CO_2 have high quadrupole moments, which can cause additional uncertainties. Namely, due to the quadrupole moment, the orientation of a molecule depends on the surface chemistry of the adsorbent. IUPAC recommends to measure gas adsorption isotherms with Ar instead of N_2, since Ar does not have a quadrupole moment and is less sensitive to differences in the structure of the adsorbent surface at experimental temperature of 87 K [26].

Compared to other gases, hydrogen diffusion is much faster and the size of the H_2 molecule is much smaller. Thereafter, H_2 can access very small micropores that are not accessible to other gases (e.g. N_2 or Ar) at cryogenic temperatures [37,38]. When H_2 isotherms are measured at 77 K (i.e. at temperature higher than the critical temperature of H_2, 33.15 K) the maximal pressure is limited by the instrument. Namely, the saturation pressure cannot be defined for hydrogen at 77 K since H_2 will not liquefy, but will become supercritical at pressures higher than 12.96 bar.

Table 1. The differences in the gas adsorption analysis conditions for different gases used [36,38].

Gas	T_m / K	$p°$ / mbar	$p/p°$ of ads./ unitless	Pore range / nm
N_2	77	1019	$\sim10^{-7}$	$0.7 < w < 50$
Ar	87	1003	$\sim10^{-6}$	$0.7 < w < 50$
CO_2	273	34853	$\sim10^{-4}$	$0.4 < w < 1$
H_2	77	–	$\sim10^{-5}$	$w < 0.7$

T_m – measurement temperature, $p°$ – the saturation pressure at atmospheric pressure and at the measurement temperature, $p/p°$ of ads. – the relative pressure at which the adsorption in micropores starts, w – pore width.

Methods based on Non-local-density functional theory (NLDFT) can be used to calculate the pore size distribution of the adsorbent based on the characteristics and the shape of the isotherm. Namely, NLDFT is used to calculate a set of theoretical isotherms for a given class of adsorbent/adsorptive system with different pore widths. This set of theoretical isotherms, the so-called kernel is then used as a reference when analysing the real measured isotherm, enabling to estimate the pore size distribution [26,39].

Conventional NLDFT models assume a smooth and homogeneous surface of the adsorbent, which is rarely realistic in the case of porous carbon materials. This drawback has been addressed by the two-dimensional NLDFT (2D-NLDFT) approach [39] and the quenched solid DFT (QSDFT) approach [40], which take into account the heterogeneity of the adsorbent surface. The 2D-NLDFT allows for the non-uniformity of the adsorbent surface in two dimensions, i.e the surface of pore wall is treated as randomly wrinkled graphene sheet containing non-hexagonal defect rings. The QSDFT describes the adsorbent and the adsorbate density in the pores in one dimension, which is perpendicular to the pore wall (same as the conventional NLDFT). However, as opposed to the conventional NLDFT method, the QSDFT model assumes that the density of carbon atoms linearly decreases to zero within the surface layer (i.e. the quenched component). It has been shown, that the QSDFT and the 2D-NLDFT methods both give similar pore size distributions despite having different mathematical ways of taking into account the heterogeneity of the surface of the adsorbent [41]. In summary, the application of advanced methods based on DFT leads to reasonably accurate evaluation of the pore size distribution, if the porous system is compatible with the chosen kernel [26].

4.2.2. Raman spectroscopy

Raman spectroscopy is widely used as a quick, non-destructive characterization method to characterize the structure of carbon materials of vastly different types, e.g. graphene, amorphous carbons, highly ordered pyrolytic graphite, etc. The first-order Raman spectra of disordered graphite typically contains two relatively sharp modes, the G (i.e. graphitic) peak around 1580–1600 cm^{-1} and the D (i.e. disorder-induced) peak around 1350 cm^{-1}. These bands are assigned to zone center phonons of E_{2g} symmetry and K-point phonons of A_{1g} symmetry (Figure 5a), respectively [42]. The G and D peaks[3] with varying intensity, width and position, also dominate in the Raman spectra of nanocrystalline sp^2 carbons (Figure 5b) [1].

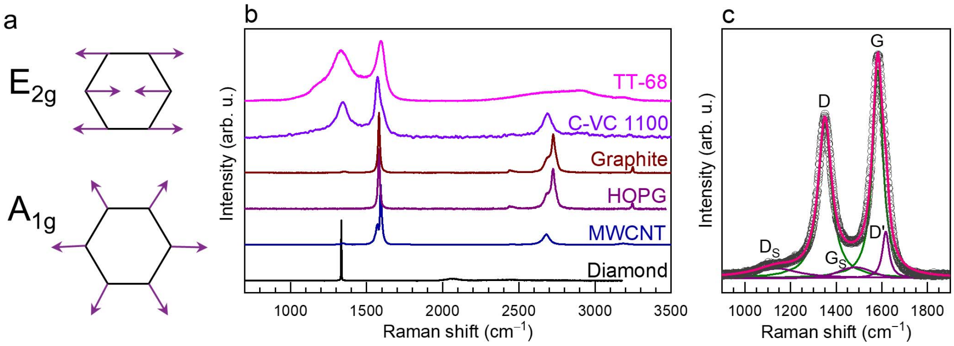

Figure 5. (a) Carbon motions in the G and D modes of graphene, E_{2g} and A_{1g}, respectively. (b) Raman spectra of various carbon materials, MWCNT – multi-walled carbon nanotube, HOPG – highly ordered pyrolytic graphite, C-VC 1100 – porous carbon synthesized from vanadium carbide at 1100 °C, TT-68 – porous carbon synthesized from D-glycose with hydrothermal carbonization and, thereafter, activated with $ZnCl_2$[4]. (c) Different bands in the first order region of the Raman spectra of Mo_2C-derived carbon.

While it is simple to distinguish between vastly different carbon samples (e.g between graphite and diamond) with Raman spectroscopy (Figure 5b), the differences in the spectra of microporous disordered carbons are more complicated to distinguish. Schuepfer et al. devised a useful classification of sp^2 carbons along the graphitization pathway based on the Raman spectra (Table 2) [43]. This classification can be used without the deconvolution of the spectra.

[3] It is not entirely correct to name the wide and overlapping bands at ~1580–1600 cm^{-1} and at ~1350 cm^{-1} in the spectra of disordered carbon G-band and D-band, respectively, since this nomenclature is meant to describe crystalline graphene and graphite. However, this notation is abundantly used in the literature so the same notation will be used in this work.

[4] Data measured by Tavo Romann from the Institute of Chemistry of the University of Tartu.

Table 2. Classification of sp^2 carbons along the graphitization pathway based on the features of the corresponding Raman spectra devised by Schuepfer et al. [43].

Stage	Name	I_D/I_G ratio	Other
I	Disordered[5]	Increases with increased graphitization, but does not exceed a value of 1.	D- and G-bands are broad and overlapping.
II	Nanoparticular	Increases further, reaches its maximum value	D- and G-bands are narrower. D′ might become visible at ~1620 cm^{-1}
III	Non-graphitic	Decreases towards zero	D- and D'-bands eventually dissapear.
IV	Graphitic	Zero.	Spectral shape of the 2D-band changes.

I_D/I_G – the ratio of the intensities (heights) of the D- and G-band, without the deconvolution of bands.

The sp^2 carbon materials typically used as supercapacitor and PEMFC electrode materials are either Stage I or Stage II carbons. In order to analyze the differences of these materials in more detail, it is nessesary to obtain comparable spectral parameters like the widths, positions and areas of the bands. The spectral parameters shown to be the most useful to characterize and/or compare the Raman spectra of disordered carbons are shown in Table 3.

In order to obtain the spectral parameters, the spectrum needs to be deconvoluted since the D- and G-bands are wide and overlapping. Moreover, in addition to the D- and the G-band, the first order Raman excitation region contains at least two to three additional bands (at ~1100 cm^{-1}, ~1450 cm^{-1} and 1620 cm^{-1}) [44–47]. The first two of these additional bands (~1100 cm^{-1} and ~1450 cm^{-1}) have been interpreted as being analogous to the D- and the G-band, but originating from the highly disordered areas (the area near the edges of the graphene domains and the areas near defects), which results in the softening of the phonon modes and, thus, the presence at lower frequencies [45]. The bands at ~ 1100 cm^{-1} and ~1450 cm^{-1} will be henceforth denoted as D_S and G_S, respectively. The third, i.e. the D'-band at ~1620 cm^{-1}, is assigned to E'_{2g} [48] and has been argued to be present in the first-order region even if a separate tip is not seen in the spectrum (Figure 5c) [46,47].

[5] The term „amorphous carbon“ was used in the original publication, but this refers to carbons with considerable sp^3-content according to IUPAC [9].

Table 3. Spectral parameters obtained from the spectra of disordered carbons. The I_D/I_G is obtained directly from the spectrum, i.e. without deconvolution, other parameters are obtained from the deconvolution results.

Spectral parameter		Notes and Ref.
I_D/I_G	The ratio of the intensities (mostly in the literature as band heights) of the D and the G band.	The value of I_D/I_G first increases and only then decreases along the graphitization pathway [1,43].
$A_{\Sigma D}/A_{\Sigma G}$	The ratio, where the sum of the areas (i.e the integrated intensities) of the ~1100 cm^{-1} band and D-band is divided by the sum of the areas of the ~1500 cm^{-1} band and the G band.	The value of $A_{\Sigma D}/A_{\Sigma G}$ decreases along the graphitization pathway. This parameter was said to be applicable for carbons with $L_a >$ 32 nm [45].
Γ_G	The full width at half maximum of the G-band.	For very disordered carbons, Γ_G is constant around ~55 cm^{-1} [49], but decreases eventually along the graphitization pathway and reaches the minimum value of 13.5 cm^{-1} in the case of highly ordered graphite [45].
Γ_D	The full width at half maximum of the D-band.	Γ_D decreases substantially along the graphitization pathway, i.e the change of Γ_D is very prominent for disordered Stage I and II carbons [47,49].

There are empirical equations, which enable to calculate the size of the carbon sheet (i.e. the graphene domain) on the basis of the I_D/I_G ratio [1,42]. However, this calculation has been shown to lead to highly unreliable results, since the defect formation and its evolution with size strongly depends on the precursor and the carbonization procedure [43,44]. It must be kept in mind, that Raman spectroscopy is a vibrational spectroscopy, not a microscopy, and the relations between the domain size and the spectral parameters are indirect. Thereafter, the most reliable results can be obtained when a series of synthesized carbons (e.g. the only variable is the heat treatment temperature) is under study [43].

The Raman linewidth depends on the disorder of the nearest-neighbor environment and the size of the sp^2 carbon domains formed, in particular for small sheet sizes. When the graphene domains in the sample are very small, the Raman spectrum can mainly consist of the contributions of various molecule-like units. Molecules do not possess translational symmetry and do not exhibit defects as crystalline materials. Nevertheless, larger units of 6-fold carbon rings may exhibit a molecular vibrational mode in the region of the D-band [50]. The lower limit, at which the graphene domain is considered to be large enough to show crystalline behaviour, has been estimated to be near the average graphene layer extent of 2 nm in [1] or 4 nm in [43] (Figure 6).

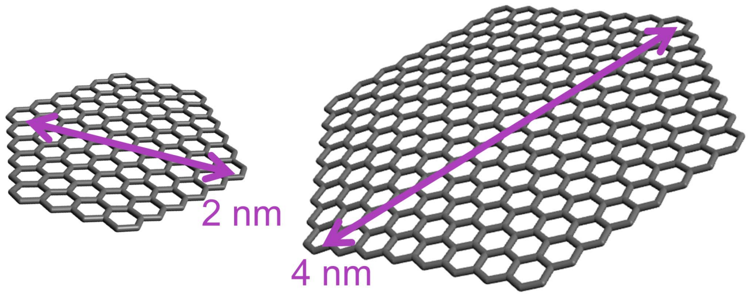

Figure 6. Representations of graphene domains with a diameter of approximately 2 nm and 4 nm, respectively.

4.2.3. Wide-Angle X-Ray Scattering

The maxima in the X-ray diffraction (XRD) pattern results from constructive interference between X-ray waves that have elastically scattered from different lattice planes. The condition for constructive interference at a certain angle is given by the Bragg equation [51]:

$$\mathrm{n}\lambda = 2d\ \sin\theta, \tag{2}$$

where n is an integer, λ is X-ray wavelength, d is the distance between lattice planes and θ is the diffraction angle. Unlike samples normally studied with XRD, the porous disordered carbons cannot be taken as truly crystalline. Thus, it is more accurate to name this method Wide-Angle X-ray Scattering (WAXS) [52].

In a WAXS pattern of microporous carbon, typically wide and diffuse (00*l*) and (*hk*) interference maxima are seen, but no well-expressed (*hkl*) reflections (Figure 7). This indicates a random layer structure, in which single graphene layers are stacked roughly parallel and nearly equidistant, but with layers having a random orientation (also known as 'turbostratic' disorder) [14]. The existance of (*hkl*) reflections is the indicator, that the carbon material is graphitic and contains three-dimensional periodicity, while non-graphitic carbons only have two-dimensional periodicity. When a non-graphitic carbon material is heat-treated at a high temperature (~2000 °C), the (*hkl*) lines can appear in the WAXS pattern (i.e. 3D order is established) and the starting carbon material is then said to be *graphitizable* or "soft" carbon. If the carbon material will not show signs of 3D order even after heating it at ~3000 °C, it is said to be a *non-graphitizable* or "hard" carbon, respectively [17].

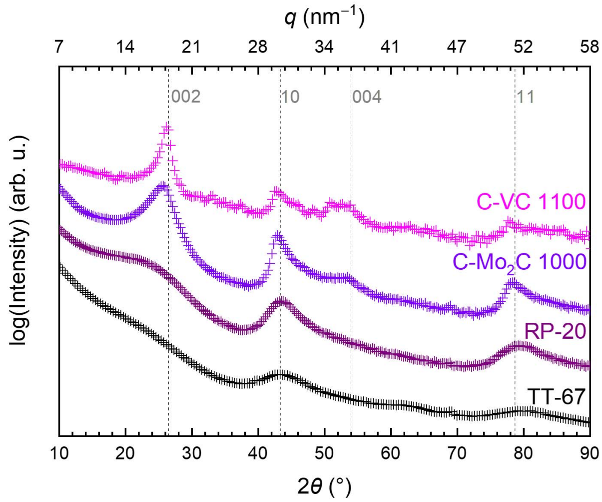

Figure 7. WAXS patterns of various sp^2 carbon materials[6]. The dashed vertical lines represent the positions of reflections in the XRD pattern of graphite. There are examples of carbide-derived carbons (C-VC 1100 and C-Mo_2C 1000 [22,23]), commercial activated carbon (RP-20 [53]) and porous carbon synthesized via hydrothermal carbonization (TT-67 [19]). On the top axis, the magnitude of the scattering vector, *q*, is shown.

When a carbon material is heat-treated at higher temperatures, the small ordered domains grow larger and, as a result, the 00*l* and *hk* maxima become narrower. Thereafter, the widths of the reflections have been used to quantify the extent of the ordered domain, L_a, according to the Scherrer equation [54].

This calculation is based on the assumption that the broadening of the interference maxima is only caused by the limited graphene domain size. However, the defects, curvature, strain etc. also affect the width of the interference maxima. In addition, the extraction of the width of the asymmetrical (10) reflection, which often partly overlaps with the (002) maxima, is riddled with uncertainties. In these cases, a fitting methods for the whole scattering curve are more appropriate [55–58].

Rietveld refinement [59] is the commonly used method to quantitavely analyze the full profile of an X-ray diffraction pattern of a crystalline sample. This algorithm optimizes the positions of atoms within the 3D unit cell in order to calculate the theoretical pattern, which is thereafter step-by-step made to resemble the measured pattern. However, since the sp^2 carbon materials contain platelets of graphene, which are mostly not interconnected with chemical bonds, the stacking disorder is common even in highly graphitic materials [14,17,60]. Therefore, neither the unit cell nor the Rietveld method are able to model the stacking of the graphene layers properly.

6 Data measured by PhD Jaan Aruväli in the Department of Geology of the University of Tartu.

Shi and Dahn [55] devised an algorithm similar to the Rietveld refinement, but with improved consideration for the stacking disorder in graphitic carbons. This algorithm takes into account the disorder of stacking, the fluctuations of interlayer spacing and the strain using a total of 18 adjustable parameters. The algorithm has been implemented in the program CarbonXS (available at *https://lktsui.github.io/carbon_xs_gui/*) [55,60].

Ruland and Smarsly [56] derived another algorithm to specifically characterize the full profile of the WAXS pattern of non-graphitic carbon materials. This algorithm has 16 adjustable parameters and is implemented in the program CarbX (available at *https://www. uni-giessen.de/CarbX*) [61]. Some of the parameters that can be calculated with this algorithm are shown in Table 4.

Table 4. Some parameters, which can be calculated with the program CarbX on the basis of the WAXS pattern of a carbon material [52].

Parameter	Denotation	Explanation
L_a	Average graphene layer extent	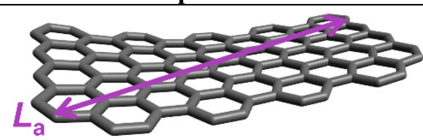
l_{cc}	Average C-C bond length	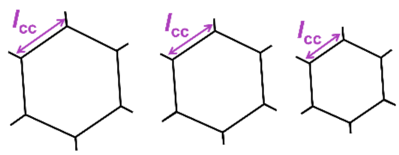
σ_1	Standard deviation of the first-neighbor distribution	
L_c	Average stacking size	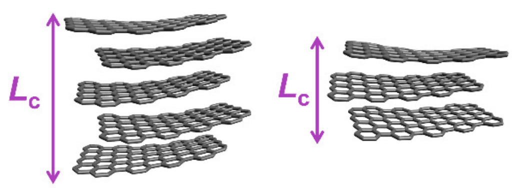
a_3	Average interlayer spacing	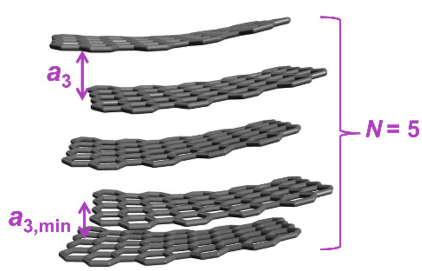
σ_3	Standard deviation of interlayer spacing	
N	The average number of layers in a stack.	

The algorithm by Ruland and Smarsly has also been successfully used to analyse the wide-angle neutron scattering (WANS) data of disordered carbons [62]. The main advantage of WANS is that the interference maxima are better distinguishable at large q values in comparison with WAXS method data. Namely, the intensity of the maxima at high q values is diminished by the atomic form factor in the case of WAXS. However, it has been shown that standard laboratory WAXS instruments provide a sufficient data quality for determining important parameters (Table 4) with enough precision for a meaningful interpretation [62].

However, both the algorithms by Shi and Dahn [55] and Ruland and Smarsly [56] assume that the carbon material is homogeneous and that the graphene layers are flat. It has been shown in the literature to an increasing extent that the disordered carbons contain mostly curved layers of graphene [3,63], thus, the results from these WAXS profile interpretations must be taken with a grain of salt.

4.2.4. Small-angle X-ray/neutron scattering

Small-angle scattering (SAS) methods rely on the same physical phenomenon as the WAXS (or WANS) method, i.e. the constructive interference between particle (the X-Ray photon or neutron) waves that have elastically scattered from the sample. However, when in the case of WAXS the scattering angle, 2θ, ranges typically from 5–90°, the scattering angles with small angle scattering are in the range from 0.01 to 11° (Cu Kα radiation, λ = 1.5406 Å)[7]. Thus, according to the Bragg equation (2) the length scale of the area studied in the material is much larger in the case of SAS. Namely, the studied length scale is in the range 0.8–1000 nm. In this length scale range also microscopy (SEM, TEM) can be used to study samples, but in comparison with microscopy, the SAS gives averaged representative data about the whole sample (Table 5).

Table 5. The comparison of small-angle scattering with microscopy in terms of what information can be extracted [64].

Feature	Microscopy	Scattering
Small details are	Visible	Not visible
Results are	Unique but not representative	Representative but ambiguous
Local structure details	Can be extracted	Cannot be extracted
Average structures are	Hard to obtain	Always obtained

[7] The scattering angle is dependent on the wavelength of the incident radiation. Therefore, it is often better to use the magnitude of the scattering vector, q, on the x-axis; $q = (4\pi/\lambda)\sin\theta$, where the λ is the wavelenth and 2θ is the scattering angle. The magnitude of the scattering vector is independent of the incident wavelength.

Both X-rays and neutrons have been used for small-angle scattering measurements on microporous carbon materials and the information received about the carbon is by-and-large similar [53,65,66]. However, there are multiple technical differences/limitations, which need to be considered when planning a SAXS or SANS experiment (Table 6). In addition, neutrons and X-rays have a different contrast due to different scattering lengths, thus, in order to plot them on the same graph, SAXS data needs to be scaled down by a factor of 6.47 in the case of materials, which only contain carbon [66].

Table 6. Some differences in the neutron and X-ray scattering experiments.

	Neutrons	**X-rays**
Experiments can be conducted	Only in large scale facilities	Both lab-scale and large-scale instruments exist
Scattering from	Atomic nuclei	Electrons
Destructivity	Non-destructive 1.5 Å neutron has an associated energy of E_n = 0.036 eV.	Destructive 1.5 Å X-ray has an incident energy, $E_{X\text{-ray}}$ = 8265 eV.
Contrast matching	Easily achieved with deuterated solvents. Deuterated toluene, D_2O, deuterated p-xylene etc. have beed used as contrast matching agents for porous carbons [29,31,53,67].	Possible, but often more complicated. Sulfur has been used as contrast matching agent for porous carbons [68,69].
Signal-to-noise	Incoherent scattering may limit resolution at high scattering angles even in the case of deuterated samples [66,70].	Owing to the absence of incoherent scattering, the resolution is higher. Possible to measure up to q = 9 nm^{-1} with a better signal-to-noise ratio [66,71].

The SAS intensity, $I(q)$, is the number of photons/neutrons of a given wavelength per unit time scattered by a sample into a detector subtending a solid angle $\Delta\Omega$ at scattering vector q. $I(q)$ contains information about the macroscopic differential scattering cross section of the sample, $\mathrm{d}\Sigma/\mathrm{d}\Omega(q)$, but is also influenced by the incident photon/neutron flux per unit wavelength, detector efficiency, sample transmission, sample volume etc. [72]. After data treatment and normalization, $\mathrm{d}\Sigma/\mathrm{d}\Omega(q)$ is obtained from the measured $I(q)$. $\mathrm{d}\Sigma/\mathrm{d}\Omega(q)$ is the Fourier transform of the electron density-density correlation function in the case of SAXS and neutron scattering length density-density correlation function in the case of SANS [64,72].

In order to analyze the macroscopic differential scattering cross section of porous carbon powders, the $\mathrm{d}\Sigma/\mathrm{d}\Omega(q)$ needs to be normalized to the apparent filling density, ρ_f, of the sample since the carbon powder does not fill the entire scattering volume,

$$\frac{d\Sigma_m}{d\Omega}(q) = \frac{1}{\rho_f}\frac{d\Sigma}{d\Omega}(q)\ , \tag{3}$$

where q is the magnitude of the scattering vector, $d\Sigma_m/d\Omega(q)$ is the normalized macroscopic differential scattering cross section in units $cm^2\ g^{-1}$. The normalization is a necessary step before any subsequent quantitative evaluation of the data. The $d\Sigma_m/d\Omega(q)$ of microporous carbons (Figure 8), henceforth noted as scattering curves, contain three regions [28].

1. Low-q region, at $q < 0.4\ nm^{-1}$ with a nearly linear decrease, which corresponds to larger mesopores and macropores.
2. Intermediate area at $0.4 < q < 3\ nm^{-1}$, which corresponds to smaller mesopores and often contains a shoulder.
3. High-q region (also known as Porod region) at $q > 3\ nm^{-1}$, that contains information on the microporous structure (< 2 nm) and the density fluctuations in the carbon, which contribute to the scattering intensity at this length scale.

In an ideal two-phase system, where the surface of the pores is smooth, the scattering in the high-q region would give rise to a dependence $d\Sigma_m/d\Omega(q) \sim q^{-4}$ (indicated as yellow dashed line in Figure 8) which is known as the Porod scattering in the literature. However, the imperfections inside and between the carbon layers due to finite size and bending of the carbon sheets leads to an additional contribution to the measured scattering curve, which decays with q^{-2} (indicated as green dashed line in Figure 8) [56,73–75]. Together with the characteristic q^{-4} Porod term, the decay of the scattering curve at high-q region will typically be in the range from q^{-2} to q^{-3}.

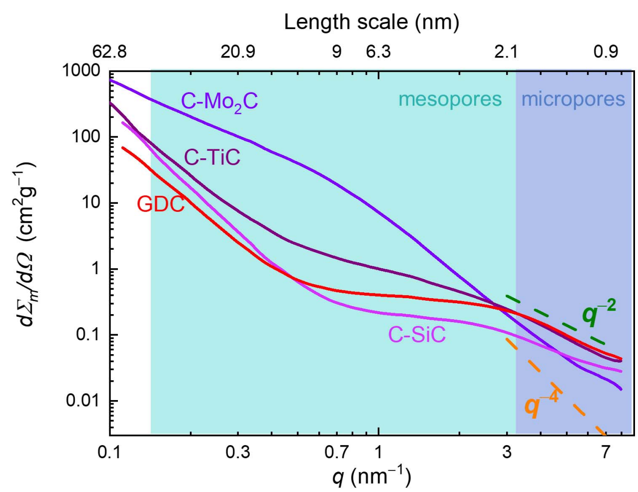

Figure 8. The mass normalized differential scattering cross section (scattering curves) of various porous carbon materials[8]. The studied length scale on the top axis is calculated by $2\pi/q$.

[8] Data is measured by PhD. Eneli Härk on V4 in HZB, Berlin.

The mass normalized differential scattering cross section from porous carbon, $d\Sigma_m/d\Omega(q)$, can be expressed in good approximation as

$$\frac{d\Sigma_m}{d\Omega}(q) = \frac{d\Sigma_{pores}}{d\Omega}(q) + \frac{d\Sigma_{fluct}}{d\Omega}(q) + C \ , \tag{4}$$

where q is the scattering vector, $d\Sigma_{pores}/d\Omega(q)$ represents the scattering between the open pores and the carbon matrix (assuming an ideal two-phase system), $d\Sigma_{fluct}/d\Omega(q)$ is the scattering originated from the density fluctuations and inaccessible pores in the carbon matrix [74], constant background C describes the q-independent 3D density fluctuations of an amorphous phase and/or the incoherent scattering background [53,67,73]. Equation (4) is based on the assumption that no strong correlation exists between the density fluctuations in graphitic-like domains and the pores.

In order to be able to analyze the scattering from the pores, $d\Sigma_{pores}/d\Omega(q)$, it is necessary substract the component $d\Sigma_{fluct}/d\Omega(q)$ from the total scattering curve, $d\Sigma_m/d\Omega(q)$. Different approaches can be used to evaluate the $d\Sigma_{fluct}/d\Omega(q)$ component of the total scattering. In the case of neutron scattering, contrast matching with deuterated solvents can be conducted to selectively "hide" the $d\Sigma_{pores}/d\Omega(q)$ component. In other words, the contribution of $d\Sigma_{pores}/d\Omega(q)$ in (5) will vanish when the pores are filled with a fluid which has the same scattering length density (SLD) as carbon (e.g. deuterated toluene, D_2O, deuterated p-xylene) and only the $d\Sigma_{fluct}/d\Omega(q)$ component will be measured [29,67]. With an elaborate experimental setup, step-by-step partial filling of pores by the contrast matching liquid has also been conducted [66,67].

The experimentally determined $d\Sigma_{fluct}/d\Omega(q)$ can be subtracted from $d\Sigma_m/d\Omega(q)$, resulting in the term $d\Sigma_{pores}/d\Omega(q)$. Thereafter, in a simplified approach the scattering from the pores, $d\Sigma_{pores}/d\Omega(q)$, is approximated as scattering from monodisperse centro-symmetric scatterers. Then, the differential scattering cross-section of pores can be written:

$$\frac{d\Sigma_{pores}}{d\Omega}(q) = N_p V_p^2 \left(\rho_p - \rho_c\right)^2 P(q) S(q) \tag{5}$$

where N_p is the number of pores, V_p is the volume of pores, ρ_p and ρ_c are the scattering length densities of pore and carbon, respectively, $P(q)$ is the form factor and $S(q)$ is the structure factor for the pores [31,76–78]. Then, the combination of power law behaviour, which is assigned to the structure factor of pores $S(q)$ [31,67,79], and the generalized Guinier-Porod model [80] can be used to obtain information about the radius of gyration and the dimensionality of the pores (i.e. average shape) etc. as done in [29]. However, it should be noted that the the generalized Guinier-Porod model assumes relatively dilute system of voids with a very well-defined shape and a specific size distribution [80].

In another analysis approach, derived by Perret, Ruland, Smarsly et al. [66,73,81,82], the fluctuation term, $d\Sigma_{\mathrm{fluct}}/d\Omega(q)$, in (4) is approximated as

$$\frac{d\Sigma_{fluct}}{d\Omega}(q) = \frac{B_{fl} l_R^2 (18 + l_R^2 q^2)}{(9 + l_R^2 q^2)^2}, \tag{6}$$

where q is the scattering vector, l_R the Ruland length describes size of laterally correlated graphene layer (correlation is lost e.g. by finite size or bending of the carbon layers) and B_{fl} defines the scattering contribution of the carbon phase, which becomes dominant at large q-values. The term l_R is adjusted so that the scattering contribution $d\Sigma_{\mathrm{fluct}}/d\Omega(q)$ does not exceed the overall scattering, i.e. $d\Sigma_m/d\Omega(q) > d\Sigma_{\mathrm{fluct}}/d\Omega(q)$ for all q values studied and analyzed.

B_{fl} can be estimated from the plot $d\Sigma_m/d\Omega(q)$ vs q^4, where at large q values the modified Porod's law applies:

$$\frac{d\Sigma_m}{d\Omega}(q) \xrightarrow[qL \gg 1]{} \frac{(2\pi)^4 P_m}{q^4} + \frac{B_{\mathrm{fl}}}{q^2} + C, \tag{7}$$

where L is the structural length scale to be analyzed and P_m is the modified Porod's constant. The fit of the modified Porod's law is carried out by plotting of $q^4 \cdot d\Sigma_m/d\Omega(q)$ vs q^2 (i.e. the modified Porod's plot).

$$q^4 \frac{d\Sigma_m}{d\Omega}(q) = (2\pi)^4 P_m + B_{\mathrm{fl}} q^2 + C q^4 \tag{8}$$

When the fluctuation term $B_{\mathrm{fl}} \cdot q^2$ is dominant ($B_{\mathrm{fl}} \cdot q^2 >> C \cdot q^4$) the the equation (8) results in a straight line in the high-q region of the modified Porod's plot. A non-zero contribution of C will result in a parabolic shape of the $q^4 \cdot d\Sigma_m/d\Omega(q)$ vs q^2 plot [53].

In this approach, the substraction of the contribution of $d\Sigma_{\mathrm{fluct}}/d\Omega(q)$ from the $d\Sigma_m/d\Omega(q)$ is considered successful, when the decay of the the $d\Sigma_{\mathrm{pores}}/d\Omega(q)$ term in the high-q region is q^{-4}, which is characteristic of an ideal two-phase system with sharp boundaries. This is a prerequisite for the following steps, where the $d\Sigma_{\mathrm{pores}}/d\Omega(q)$ is analysed by the chord length distribution (CLD) [83]. The advantage of the CLD analysis approach is the possibility to calculate the average pore sizes and the pore wall thicknesses without assuming a certain pore morphology [82]. However, from an experimental point of view, it has been shown, that the interpretation of SAXS/SANS data from carbons via CLD analysis requires a sufficient range of accessible scattering angles up to approximately $q = 9.53\ \mathrm{nm}^{-1}$ [82][9]. The data quality in the high-q region is of utmost importance to ensure an unambiguous interpretation of the Porod regime and deviations from the Porod's law.

[9] In the original publication the scattering vector is defined as $s = (2/\lambda)\sin\theta$ as opposed to the definition $q = (4\pi/\lambda)\sin\theta$ used elsewhere in this thesis; thus they cited $s = 1.5\ \mathrm{nm}^{-1}$ as the necessary maximum scattering vector.

Chord length distributions, $g(r)$, describe the shape, size and spatial arrangement of geometrical objects (e.g. pores, particles) (Figure 9a). In principle, the CLD is proportional to the second derivative of the correlation function of small-angle scattering curve and it can be calculated from the Fourier transform of the $d\Sigma_{pores}/d\Omega(q)$ term [82,84]. If the porosity is much smaller than 50%, the chord length distribution, $g(r)$ may be viewed as characterizing mainly the lengths of chords passing through pores [85]. Otherwide, the $g(r)$ is composed of the distribution of chords inside the pores and the pore walls, respectively (Figure 9b). When these distributions overlap, the CLD will contain a single positive peak. Nevertheless, the position of the peak(s) in the CLD does not give the average spatial dimensions of the pores and pore walls [84].

The CLD at small length scales and the value $g(0)$ reflect the topological properties of the interface such as curvature and angularity. Namely, a value of $g(0) > 0$ is indicative of angular structures (e.g. edges, vertices) and $g(0) = 0$ for spheres (Figure 9a) [86,87]. The CLD has been used to analyze the SAS curves of different microporous, non-graphitic carbons in [30,53,66–68].

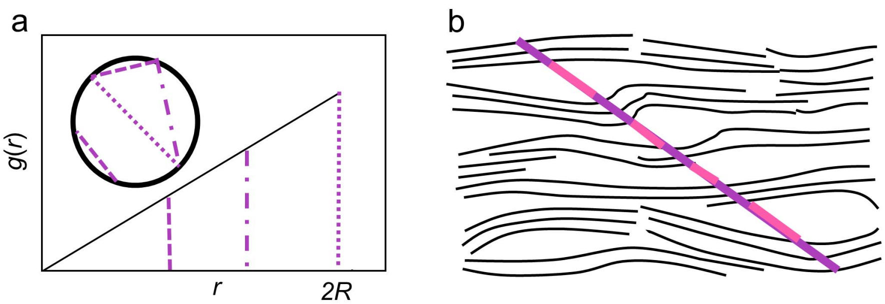

Figure 9. (a) Example of a chord length distribution, $g(r)$, of a sphere with a radius R [85]. (b) The structure of microporous carbons in terms of the chord length distribution. Some of the chords go through the solid pore walls (violet lines) and some go through the pores (pink lines) [67].

4.3. Quasi-elastic neutron scattering

The wavelength and energy of neutrons in scattering experiments ranges from 0.5 to 20 Å and 0.2 to 330 meV, respectively. Consequently, neutrons yield simultaneously information about the structure of the sample in the atomic to nanometer length scale and the dynamic processes taking place in the sample (e.g. diffusion, lattice vibration) [33,88].

The change in the momentum (9) and energy (10) of the incident neutron due to scattering are expressed as:

$$\boldsymbol{q} = \boldsymbol{k}_f - \boldsymbol{k}_i \tag{9}$$

$$\Delta E = \hbar\omega = E_f - E_i \tag{10}$$

where $\boldsymbol{q}$ is scattering vector, which describes the momentum transfer, $\boldsymbol{k}_f$ and $\boldsymbol{k}_i$ are the wave vectors of the final and incident neutron, respectively. ΔE is the energy transfer, ħ is the angular Planck's constant, ω is angular frequency, E_f and E_i are energies of final and incident neutron, respectively. When the lengths of the final and initial wave vectors are equal (i.e. $k_f = k_i$) and $\Delta E = 0$, the scattering of the neutron is considered elastic, otherwise inelastic. Quasi-elastic scattering is inelastic scattering, where the peak maximum is situated at $\Delta E = 0$ and the energy transfer is very small, typically $\Delta E \leq 2$ meV [88].

Scattering of a neutron from an atom can be coherent or incoherent. If the scattering is coherent, the neutron wave interacts with the whole sample as a unit and the scattered waves from different nuclei interfere with each other. It is the coherent scattering that is interpreted and analyzed in the case of WANS and SANS. In the case of incoherent neutron scattering, a neutron wave interacts independently with each nucleus in the sample. Thereafter, there is no interference of waves scattered from different nuclei. The dynamics, which are associated with the incoherent scattering are related to uncorrelated self-motion, like diffusion [33,88].

Hydrogen has a large incoherent neutron scattering cross-section (σ_{inc} = 80.26 barn) and a small coherent scattering cross-section (σ_{coh} = 1.76 barn). Thus, when the sample contains H_2, the coherent scattering contribution can be considered negligible and only the incoherent contribution has to be taken into account.

Quasi-elastic neutron scattering experiments, which investigate the uncorrelated self-motion, are set up in a way that enables to ignore the coherent scattering signal and focus on the incoherent scattering signal. In this case, the experimentally measured dynamic structure factor, $S_{exp}(\boldsymbol{q}, \Delta E)$, is proportional to the convolution of the incoherent dynamic structure factor $S_{inc}(\boldsymbol{q}, \Delta E)$ with the resolution function of the instrument, $R(\boldsymbol{q}, \Delta E)$. The $S_{inc}(\boldsymbol{q}, \Delta E)$ contains information about the uncorrelated self-motion dynamics in the sample. The $R(\boldsymbol{q}, \Delta E)$ of a QENS instrument determines the slowest dynamics that are possible to be studied. Typically, the width of the resolution function is near 0.1 meV. The narrower the resolution function, the slower motions can be studied. The length scale investigated with QENS is determined by the incident neutron wavelength, λ, since the momentum transfer q is set by $q = 4\pi\lambda^{-1}$ [33,89].

Self-diffusion, which is too slow to be determined given the experimental resolution, will result in a component shaped like the resolution-funtion (e.g. the Gaussian function) in the $S_{inc}(\boldsymbol{q}, \Delta E)$. Self-diffusion, which takes place at the optimal temporal window (not too slow, not too fast), will typically result in a Lorentzian-shape component in the $S_{inc}(\boldsymbol{q}, \Delta E)$, also named the quasi-elastic broadening of the signal. Motions, which are too fast to be determined given the temporal window of a QENS instrument, will contribute to the baseline of $S_{inc}(\boldsymbol{q}, \Delta E)$ [33,89].

If the self-diffusion is unrestricted, the diffusion follows the Fick's law, i.e. the width of the quasi-elastic broadening, Γ_{QE}, depends linearly on q^2. In most cases, at low q values (i.e. bigger length scales) the dependence follows the

Fick's law. If at higher q values the dependance of Γ_{QE} on q^2 deviates from linear, more complex self-diffusion mechanisms, e.g. jump-diffusion between different adsorption sites are taking place [33]. Few examples of jump-diffusion models are the Chudley-Elliot [90], Hall-Ross [91] and Singwi-Sjölander [92] models, which assume a constant jump length, a gaussian and an exponential distribution of jump lengths, respectively (Figure 10c).

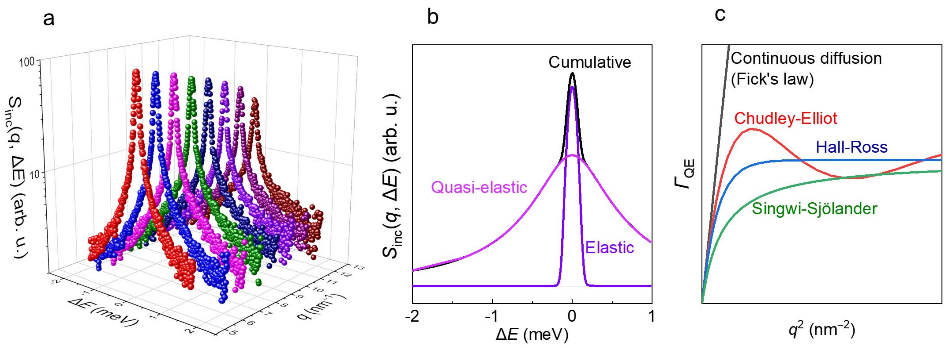

Figure 10. (a) The three-dimentional function $S_{inc}(q, \Delta E)$[10]. (b) Deconvolution of $S_{inc}(q, \Delta E)$ into an elastic and quasi-elastic component. (c) Different Γ_{QE} vs q^2 relations, which correspond to different mechanisms of diffusion (noted in Figure).

[10] Data measured on the instrument FOCUS, PSI Switzerland, on C-SiC 1000 with H_2 loading pressure of 1 bar at 90 K by Heisi Kurig, Eneli Härk and Margarita Russina.

5. EXPERIMENTAL

5.1. Gas adsorption analysis

The adsorption/desorption measurements were conducted on the instrument ASAP 2020 (Micromeritics, USA). Different gases used were N_2, CO_2, Ar and H_2 at temperatures 77 K, 273 K, 87 K and 77 K, respectively.

All pore-size distributions were calculated using the numerical algorithm SAIEUS [93,94] which solves the adsorption integral equation utilizing splines and is based on the 2D-NLDFT calculations. 2D-NLDFT Heterogeneous surface kernels "Carbon-N2-77, 2D-NLDFT Heterogeneous Surface", "Carbon-CO2-273, 2D-NLDFT Heterogeneous Surface" and "Carbon-Ar-87, 2D-NLDFT Heterogeneous Surface" were applied to N_2, CO_2 and Ar isotherms, respectively. When possible, dual gas analysis was used combining CO_2 isotherm data with either N_2 or Ar adsorption data.

5.2. Raman spectroscopy data

The CDC samples of which the Raman spectra was analyzed are given in Table 7.

Table 7. The precursor carbides and corresponding chlorination temperatures of carbide-derived carbon powders for which the Raman spectra were analyzed.

Precursor carbide	Chlorination temperature (°C)							Ref.
Mo_2C		600	700	800	900	1000	1100	[22]
Ta_4HfC_5				800	900	1000	1100	[24]
$WTiC_2$				800	900	1000	1100	[24]
WC				800	900	1000	1100	[95]
TiC				800	900	1000	1100	[96]
VC	500	600	700	800	900	1000	1100	[23]

Raman spectroscopy measurements were conducted on an inVia micro-Raman spectrometer (Renishaw, Kingswood, UK) with excitation wavelength, λ_L, 514 nm. While measuring the spectrum, the incident power was kept low (~1 mW at the sample). Each spectrum analyzed represents the average of at least three measurements from different regions selected on the same sample. OriginPro 2019b (OriginLab, San Francisco, CA, USA) was used to analyze and deconvolute the spectra.

Prior to deconvolution, the baseline (4th order polynomial function) has been subtracted from the spectrum under analysis. The first order Raman spectra was deconvoluted using four different approaches (Table 8). For more details the reader is referenced to [97].

Table 8. Different deconvolution approaches for the first-order Raman spectra.

Denotation	Description	Ref.
L+L+BWF	Two Lorentzian distribution functions centered at ~1350 cm^{-1} and a Breit-Weigner-Fano function centered at ~1500 cm^{-1}.	[49]
G+L+G+L	Two Lorentzian functions centered at ~1350 cm^{-1} (i.e, the D-band) and 1500 cm^{-1}, (i.e. G-band) respectively, and two Gaussian functions centered at both sides of the D-band.	[45]
L+L+G+G	Two Lorentzian functions centered at ~1200 cm^{-1} and 1350 cm^{-1} and two Gaussian functions centered at ~1450 cm^{-1} and 1500 cm^{-1}.	[29]
L+L+G+L+L	Four Lorentzian functions centered at ~1200 cm^{-1}, 1350 cm^{-1}, 1500 cm^{-1} and 1620 cm^{-1} and one Gaussian function centered at ~1450 cm^{-1}.	[46]

5.3. Wide-angle X-Ray scattering data

The WAXS patterns were measured with diffractometer Bruker D8 Advance (Bruker Corporation) using Cu Kα radiation (λ = 1.5406 Å), Goebel mirror, 2.5° Soller slits and LynxEye 1D detector and Bragg-Brentano geometry. The scattering angle θ was changed in 0.025° steps in the range from $5° < 2\theta < 90°$. WAXS data was fitted with the algorithm derived by Ruland and Smarsly [56] using the CarbX software (*https://www.uni-giessen.de/CarbX*) [61].

Carbon samples of which the WAXS was measured and analyzed can be seen in Table 9 and for more details the reader is referenced to [97].

Table 9. The precursor carbides and corresponding chlorination temperatures of carbide-derived carbon powders of which the WAXS was analyzed.

Precursor carbide	**Chlorination temperature (°C)**					**Ref.**
Mo_2C		800	900	1000		[22]
Ta_4HfC_5			900	1000	1100	[24]
$WTiC_2$		800	900	1000		[24]
WC		800	900	1000	1100	[95]
TiC		800	900	1000	1100	[96]
VC	600			1000	1100	[23]

5.4. Small-angle X-ray and neutron scattering data

Measurements on C-Mo_2C 600, 700, 800, 900 and 1000 were performed on an SAXSess (Anton Paar) using slit collimation with monochromatic Cu Kα radiation (λ = 1.5406 Å) and a one-dimensional position sensitive detector (Mythen 2R, Dectris) in Helmholz Zentrum Berlin, HZB. Scattering of the samples was acquired within the range of scattering vectors $0.1 < q < 7\ nm^{-1}$. The sample chamber was evacuated to 0.5 mbar to avoid air scattering. For more details see [98].

Small-angle neutron scattering measurements C-Mo_2C 700, 800, 900 and 1000 were performed on the time-of-flight pinhole collimated V16 instrument at Helmholtz Zentrum Berlin, HZB [99]. The beam wavelength used varied in the range $2.8 \leq \lambda \leq 80$ Å and data was acquired in the scattering vector range $0.04 < q < 7\ nm^{-1}$.

Prior to measurements, the C-Mo_2C samples were degassed at 120 °C and 100 μbar for 12 h. The carbon samples were prepared inside well-treated quartz cuvettes (Hellma Analytics, Germany) with 1 mm optical path length. For more details see [100].

5.5. Quasi-elastic neutron scattering data

QENS measurements to determine the mass transfer characteristics of adsorbed H_2 in C-TiC 950 [101], C-SiC 1000 [102], and C-Mo_2C 1000 [22] were performed at Paul Scherrer Institute in Villigen, Switzerland, on the cold neutron time-of-flight spectrometer FOCUS [103] with incident neutron wavelength of 0.502 nm and the elastic energy resolution of 100 meV. A cylindrical sample holder cell made of aluminium with an inner cylinder (inner diameter of the sample was 0.555 cm and outer diameter 1.02 cm) was used for all samples.

Firstly, the outgassed carbon was measured at different temperatures to determine the background signal level, then the temperature was set at 77 K and H_2 was dosed to the sample holder. The equilibrium pressure of H_2 in the sample holder at 77 K was then established as $p_{H2,load}$ and the valve between the gas apparatus and sample holder was closed. Thereafter the sample holder was cooled down and data was collected at different temperatures ranging from 10 to 120 K. The amount of H_2 per mass of the carbon sample in the sample holder, n_{H2}, was calculated from the $p_{H2,load}$ based on the fit of the Sips equation [104] to the H_2 adsorption isotherm.

Binning of the scattering data was performed in a range of scattering vectors, q, from 2 to 24.5 nm^{-1} with a step size of 1.5 nm^{-1} and in ΔE range from −2 to 2 meV with a step size of 0.008 meV. Data reduction (i.e normalization with vanadium signal and corrections for detector efficiency and the subtraction of background) was performed with the software DAVE 2.4 [105]. Before the deconvolution of data into the elastic and quasi-elastic components, the $S_{inc}(q, \Delta E)$ of outgassed (i.e. empty) carbon signal was subtracted from the $S_{inc}(q, \Delta E)$ of carbon containing H_2. For more details on the experiment see [106].

6. RESULTS AND DISCUSSION

6.1. Wide-angle X-ray scattering

All the studied carbide-derived carbons can be classified as non-graphitic carbons based on their WAXS patterns, which do not contain any (*hkl*) reflections (some examples in Figure 11a). The average stacking size, L_c, was seen to be roughly independent of the synthesis temperature, T_{syn}, in the case of most CDCs analyzed (Figure 11b, Table 10). The exceptions are C-Mo_2C and C-VC, where L_c increases significantly with increased T_{syn}, which refers to the significant stacking of graphene sheets at higher T_{syn}. It has been shown previously, that the transition between a CDC with disordered structure and a CDC with a more crystalline structure can happen in a relatively small temperature window and that for VC this transition happens at a relatively low temperature [107].

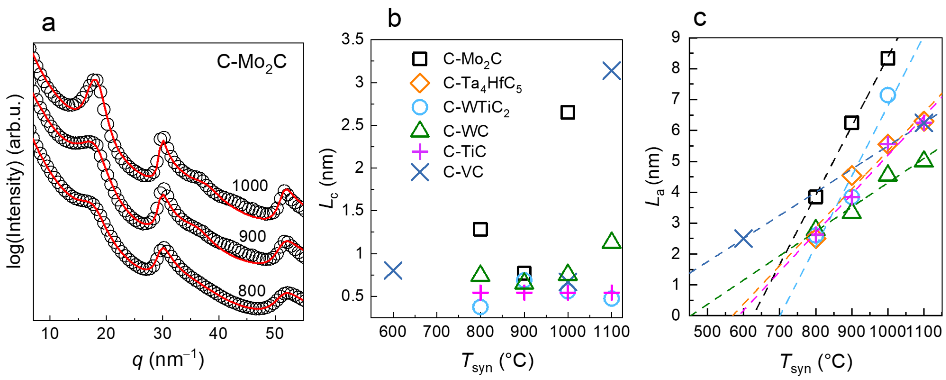

Figure 11. (a) Wide-angle X-ray scattering patterns of Mo_2C-derived carbons prepared at different synthesis temperatures (noted on Figure), the red line is the fit of the algorithm by Ruland and Smarsly [56]. (b) The L_c of CDCs plotted against the T_{syn}. (c) L_a of CDCs plotted against T_{syn}.

The average C−C bond length, l_{cc}, is near to 0.141 nm, which is characteristic of aromatic carbons. The defect density in a aromatic sp^2 carbon layer decreases with T_{syn}, which is evidenced by the decrease of the standard deviation of the first-neighbor distribution, σ_1, with T_{syn}. In addition, the extent of the graphene domain, L_a, increases with T_{syn} for all CDCs (Figure 11c). The L_a changes in the range from 2.5 to 8.3 nm (Table 10). Thus, the assumption that the L_a of CDCs is <2 nm, which was previously seen in [108], is proven to be erroneous for our dataset. The results established here are more in line with the study by Christians et al. [107], where the L_a of CDCs with similar T_{syn} values was estimated to be ~7 nm. In conclusion, as the T_{syn} increases, larger and more defect-free graphene sheets are formed in CDCs, but the number of layers in an average stack stays constant in the majority of studied materials.

Table 10. Parameters calculated with the algorithm derived by Ruland and Smarsly [56].

	$C\text{-}Mo_2C$		C-WC		C-TiC		C-VC	
T_{syn}	**800**	**1000**	**800**	**1000**	**800**	**1000**	**600**	**1100**
L_a, nm	3.8	8.3	2.8	4.5	2.6	5.6	2.5	6.3
l_{cc}, nm	0.1412	0.1410	0.1411	0.1411	0.1410	0.1414	0.1416	0.1406
σ_1, nm	0.016	0.012	0.016	0.015	0.021	0.018	0.020	0.011
$\langle N \rangle$	1.05	6.74	1.40	1.90	1.08	0.97	1.51	0.09
L_c, nm	1.28	2.65	0.55	0.75	0.50	0.59	0.82	3.14
a_3, nm	0.364	0.351	0.314	0.347	0.365	0.365	0.395	0.343
σ_3, nm	0.061	0.048	0.057	0.021	0.038	0.039	0.051	0.011

L_a – average graphene layer extent, l_{cc} – average C-C bond length, σ_1 – standard deviation of the first-neighbor distribution, $\langle N \rangle$ –average number of graphene layers per stack, L_c – average stacking size, a_3 – average interlayer spacing, σ_3 – standard deviation of interlayer spacing.

6.2. Raman spectroscopy

The Raman spectra of studied CDCs are characteristic of disordered soot-like carbons, since they mostly contain wide and overlapping D- and G-bands and more than two distribution functions are needed to deconvolute the first order region of the spectra. Based on the classification of sp^2 carbons by Schuepfer et al. [37], most of the carbons in the dataset (Table 8) can be classified as Stage I (disordered) or Stage II (nanoparticular) carbons. Only exceptions are $C\text{-}Mo_2C$ 1100 and C-VC 1100, which can be classified as Stage III (non-graphitic) carbons.

Since the spectral parameters depend on the deconvolution method used, different deconvolution approaches found in the literature were applied to the dataset (Table 7, Figure 12a−d). Although all deconvolution methods resulted in sufficiently good fits (i.e. R^2 values >0.98), these methods did not give equivalent spectral parameters (Figure 12e−h) from the investigated CDCs Raman spectra data.

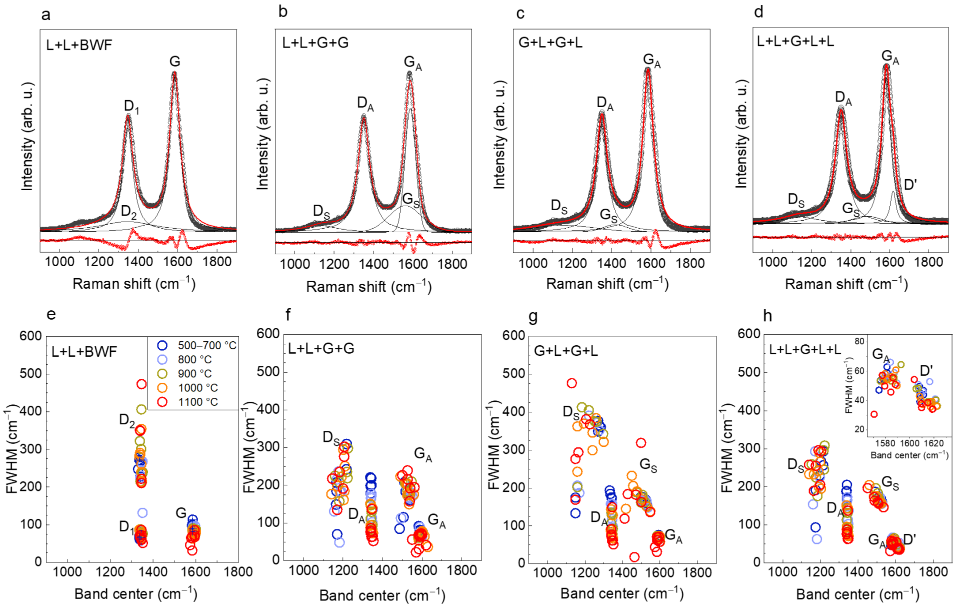

Figure 12. (a–d) The deconvolution of the first-order Raman spectrum of C-Mo_2C 1000 using different deconvolution methods (noted in Figure). Experimental spectra are given as black circles, fits are given as solid lines (orange lines for cumulative fits and black lines for single peak fits). The residuals (red dots) are plotted below the spectra. (e–h) Plots of the full width half maximum (FWHM) of the band vs the band center position data obtained by different first order Raman spectrum band deconvolution methods (noted in Figure) for CDCs synthesized at different temperatures (noted in Figure). The inset in (h) shows the zoomed in G-band region.

The main differences in the spectral parameters (band positions and widths) resulting from different deconvolution approaches can be seen by plotting the FWHM vs the band center for CDC materials under analysis (Figure 12e–h). The G- and the D-band have a well-defined band center position and width irrespective of the deconvolution method. For the 4-band deconvolution methods (Figure 12f,g) both the position and the width of the D_S, at ~1200 cm^{-1}, and G_S, at 1550 cm^{-1}, bands are widely scattered. However, the position and widths of both D_S and G_S bands are much more well-defined if the L+L+G+L+L approach is used. In case of the 5-band deconvolution approach the position of the D'-band is separated from the position of the G_A-band for the whole dataset (inset in Figure. 12h). Owing to the most accurate fit (i.e. no systematic errors seen in the residual values) and the most well-defined spectral parameter values (Figure 12d and h), only the spectral parameters from the deconvolution with five bands, L+L+G+L+L, were analyzed further.

The ratio of the D- and G-band intensities, I_D/I_G, has been widely used to characterize the relative structural order of a carbon material [1,42,107,108], but the interpretation of the I_D/I_G is not straightforward, since I_D/I_G initially increases and only then decreases along the graphitization pathway of a disordered carbon from Stage I to Stage III. Of the spectral parameters described in Table 3, the parameters $A_{\Sigma D}/A_{\Sigma G}$, and the width of the D-band showed systematic decrease with the T_{syn} (Figure 13). Since with WAXS method it was determined, that the L_a increases and the defect density decreases with higher T_{syn}, it is likely that the $A_{\Sigma D}/A_{\Sigma G}$[11] and the width of the D-band also characterize the same ordering effect. Thus, these parameters can be suitable to use as quantitive measures of the disorder in different Stage II carbon materials.

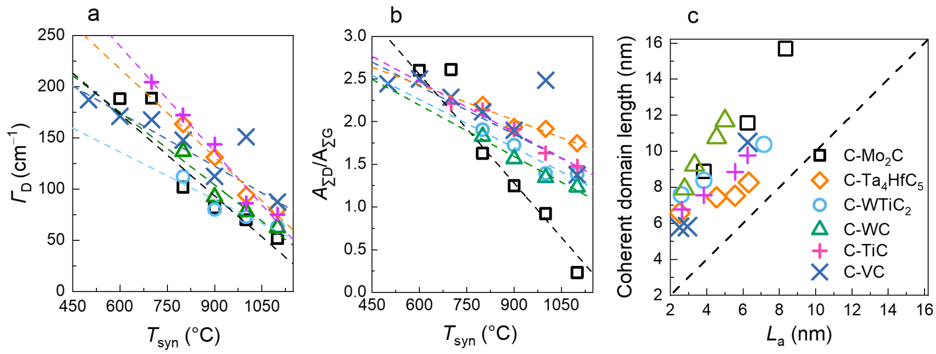

Figure 13. (a) The full-width half maximum of the D-band (Γ_D) data and (b) the ratio $A_{\Sigma D}/A_{\Sigma G}$ (Eq. 5), versus the synthesis temperature of the CDC. Lines are guides for the eye. (c) The coherent domain size calculated by $L_a = 490/E_{laser}^4 \, (A_{\Sigma D}/A_{\Sigma G})^{-1}$ [45] vs the L_a calculated from WAXS data.

Ribeiro-Soares et al. [45] proposed an equation for the calculation of the coherent domain length from Raman spectra based on the $A_{\Sigma D}/A_{\Sigma G}$ ratio. Using this equation, the coherent domain lengths for the studied CDCs are from 6 to 16 nm (Fig. 13c) and increase systematically with the increase of T_{syn} for CDCs prepared using the same precursor carbide. This proves the applicability of the equation based on $A_{\Sigma D}/A_{\Sigma G}$ ratio to characterize the structure of the studied CDCs. The coherent domain lengths calculated from the $A_{\Sigma D}/A_{\Sigma G}$ ratio are larger by 3−6 nm (average 4.4 nm) compared to the L_a established with WAXS analysis. The reason for this discrepancy might be that when a layer contains defects and/or is curved, the coherent domains seen by WAXS method are diminished, whereas phonon propagation is not stopped [109]. Especially given that the D-band is not only activated near the edge of the graphene domain, but also near different defects in the graphene domain [110]. Consequently, the coherent domains detected via Raman spectroscopy are somewhat larger in comparison to the L_a values established by the WAXS analysis method (Fig. 13c). The curved graphene layers can indeed be longer than 10 nm, as has been shown by transmission electron microscopy of CDCs (Figure 14) [95,107,108,111].

[11] In the $A_{\Sigma D}/A_{\Sigma G}$, also the area of the D′ band is taken into account, see equation 5 in [97].

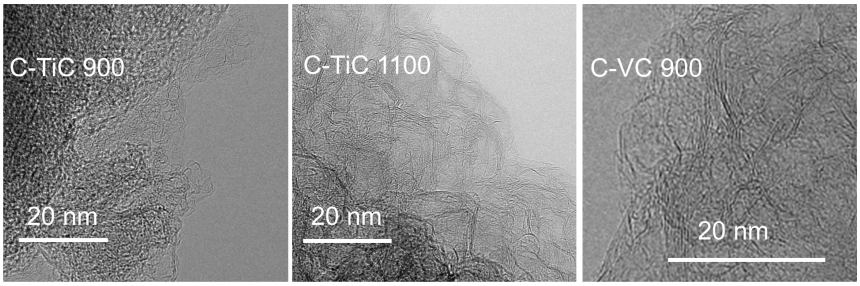

Figure 14. Transmission electron microscopy micrographs of some CDCs materials (noted in Figure)[12].

6.3. Small-angle scattering

From the scattering curves of Mo_2C-derived carbons (Figure 15a,b) it can be seen that as the T_{syn} of the carbons is increased, the scattering intensity decreases in the micropore region ($q > 3\ nm^{-1}$) and increases in the mesopore region ($0.2 < q < 3\ nm^{-1}$). The higher amount of mesopores with increased T_{syn} is also visible from the gas adsorption analysis results (Figure 15c). Similar change from prevalently microporous to prevalently mesoporous or even macroporous structure with increasing synthesis temperature of CDC has been shown previously in [107] for a large dataset of CDC materials.

For disordered porous carbons, it is characteristic that the decay of scattering intensity in the high-q region is in the range of q^{-2} to q^{-3} (Figure 15a), but not q^{-4}, which would indicate a smooth surface. More specifically, the exponent of decay parameter (i.e the Porod constant, d) decreases with the increase in T_{syn} according to SAS data (Figure 15a,b). This result shows that the amount of imperfections inside and between the carbon layers and also the amount of micropores decreases with the increase of T_{syn}.

For the analysis of SANS data, the generalized-Guinier Porod approach was applied (see Section 4.2.4), which assumes, that the pore shape would be cylindrical, slit-like or some combination of the shapes mentioned. The results showed, that the shape parameter s increased with the T_{syn} (Table 11), which corresponds to the transformation of Mo_2C-derived carbon from prevalently cylinder-like to prevalently slit-like structures.

For the analysis of SAXS data, the chord length distribution (CLD) analysis approach was used, which does not assume any specific shape for the pores. From that analysis, the parameter expressing the shape is the degree of anguliarity, $g(0)$, which decreases systematically with the T_{syn} of studied materials (Table 11). Thus, irrespective of the analysis approach used, the results from SAS indicate that the pore walls become less curved and contain less defects

[12] HRTEM micrographs are from Prof. K. Kontturi from the Department of Chemistry at Aalto University and previously published in [112].

(the cause for anguliarity) as the T_{syn} increases (Figure 15d). This result is supported also by Raman spectroscopy and WAXS data, which clearly indicate that the average graphene platelet size increases with T_{syn} and amount of defects decreases with T_{syn} (see previous Sections).

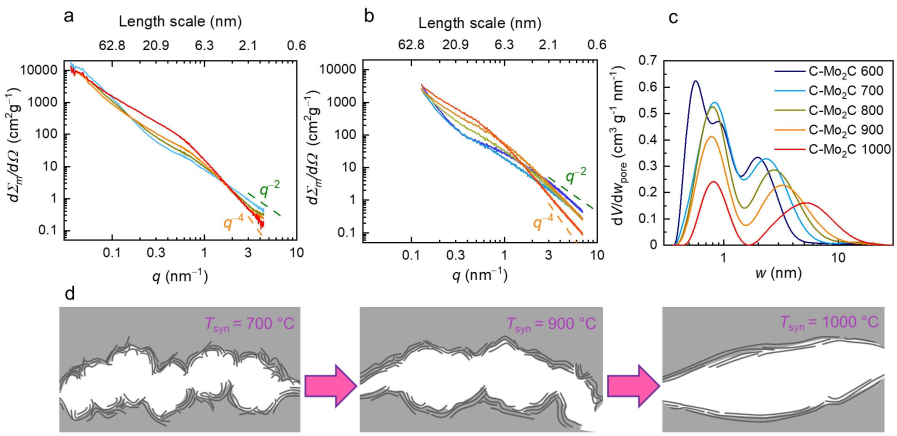

Figure 15. The scattering curves of Mo_2C-derived carbons (noted in Figure c) measured with (a) SANS [100] and (b) SAXS method [98]. (c) The pore size distributions of C-Mo_2C carbons calculated based on the CO_2 and N_2 adsorption isotherms. (d) Illustration of the change of the structure of the pore with the synthesis temperature of CDC based on SAS data for C-Mo_2C materials synthesised at different temperatures.

Comparing other parameters established with different analysis approaches for SAS data about the Mo_2C-derived carbon, it can be said that the radius of gyration, R_g, and the number-averaged chord-length, l_p^{SAXS}, are quite similar in the case of C-Mo_2C 700 and 800, both indicating that the average pore/pore wall size is in the range from 0.6 to 0.7 nm. However, a steep change in the parameters is seen when T_{syn} changes from 900 to 1000 °C (Table 11). This steep change was also seen with Raman spectroscopy, as C-Mo_2C 900 could be classified as Stage II carbon, but C-Mo_2C 1000 already belongs to Stage III region in the graphitization pathway. The probable explanation is, that the graphene platelets can coalesce and rearrange considerably more easily at 1000 °C in comparison with 900 °C in the case of C-Mo_2C, which results in larger and more defect-free graphene platelets. Larger graphene platelets give rise to larger pores with smoother surfaces (as evidenced by the Porod constant, d, in Table 11) and decreased amount of microporosity. In addition, the decrease in the amount of microporosity can be a result of more ordered stacking of graphene layers, which was evidenced by the considerable increase in the L_c parameter (Figure 11b, Table 10). Altogether, the inner surface area diminishes, which can be seen both from the S/m parameter and from the results established using gas adsorption analysis methods (Table 11).

Table 11. Different characteristics of CDCs derived from Mo_2C with varied T_{syn}.

	SANS[b]			SAXS[a]				Gas adsorption	
T_{syn} °C	R_g nm	s	d	B_{fl} $cm^2g^{-1}nm^{-2}$	S/m m^2g^{-1}	l_p^{SAXS} nm	$g(0)$ nm^{-1}	S_{DFT} $m^2\ g^{-1}$	V_{tot} $m^3\ g^{-1}$
600				10.8	965	0.57	1.24	1577[a]	1.28[a]
700	0.59	1.20	2.03	9.7	950	0.59	1.16	1665[a], 1720[b]	1.57[a], 1.61[b]
800	0.60	1.32	2.65	7.6	1310	0.72	1.13	1424[a], 1380[b]	1.65[a], 1.48[b]
900	0.65	1.46	3.10	7.9	1363	0.92	0.92	1139[a], 1280[b]	1.43[a], 1.50[b]
1000	0.73	1.75	3.40	2.23	621	1.52	0.25	734[a], 680[b]	1.42[a], 1.35[b]

R_g – radius of gyration, s – dimensionality parameter, d – Porod constant, B_{fl} – scattering contribution from disordered carbon (Eqs. 6–8), S/m – inner surface area, l_p^{SAXS} – number-average chord length and $g(0)$ – degree of anguliarity, S_{DFT} – specific surface area calculated from 2D-NLDFT model, V_{tot} – total volume of pores calculated from the amount of adsorbed gas near the saturation pressure, $p/p° = 0.95$.
[a] Results from [98], where gas adsorption analysis was done with N_2.
[b] Results from [100], where gas adsorption was done with CO_2 and Ar.

6.4. H_2 diffusion in CDCs

From the carbon materials chosen for the *in situ* QENS study on H_2 diffusion, C-SiC 1000 and C-TiC 950 were the most microporous. C-SiC 1000 contained more pores with $w < 1$ nm, but less pores with $w > 1$ nm compared to C-TiC 950. C-Mo_2C 1000 was drastically different, as C-Mo_2C 1000 is rather mesoporous and exhibits considerably lower microporosity (Figure 16a).

C-SiC 1000 and C-TiC 950 also had similar H_2 adsorption isotherms (Figure 16b). Although, more H_2 is adsorbed in C-SiC 1000 than C-TiC 950 at $p_{H2} < 0.4$ bar due to the larger amount of subnanometer pores in C-SiC 1000. However, more H_2 is adsorbed in C-TiC 950 at $p_{H2} > 0.5$ bar, where C-TiC 950 has more pores with widths 1 nm < w < 2 nm (Figure 16). Due to the lack of microporosity the amount of H_2 adsorbed in C-Mo_2C 1000 at 1.1 bar is considerably lower compared to the other CDCs under study (Figure 16b).

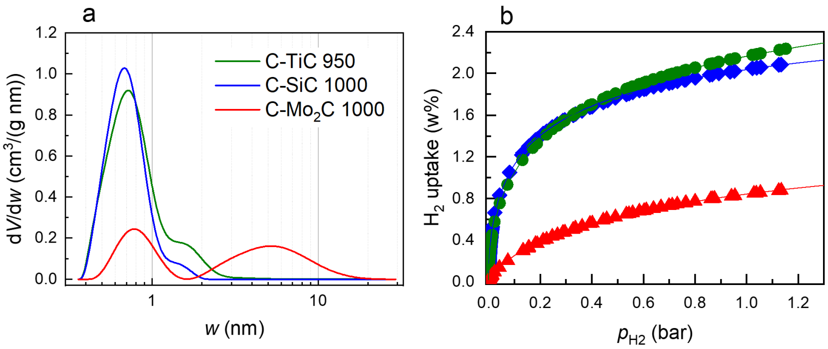

Figure 16. (a) Pore size distributions calculated according to N_2 and CO_2 isotherms for C-TiC 950, C-SiC 1000 and C-Mo_2C 1000 (noted in Figure). (b) H_2 adsorption isotherms for the same carbon materials. The solid line is the fit of the Sips equation [104].

The *in situ* quasi-elastic neutron scattering (QENS) is very sensitive towards the presence of adsorbed hydrogen and is used for the observation of molecular (self-)diffusion phenomena, which enables to investigate the strength of interaction between the adsorbent and the adsorbed species.

In the case of the lowest amount of H_2 per sample, n_{H2} = 2.4 mmol g^{-1}, only the elastic scattering component is present for C-SiC 1000 (Figure 17a). This was true for all measured temperatures, i.e. up to 120 K, which indicates that at n_{H2} = 2.4 mmol g^{-1}, hydrogen is strongly bound and practically immobile in the pores of the C-SiC 1000. As totally opposed to this, the quasi-elastic broadening, i.e. mobile hydrogen, could be detected for C-TiC at n_{H2} of 2.0 mmol g^{-1}, already at temperatures higher than 25 K (Figure 17b). In the case of C-Mo_2C 1000 and at the lowest H_2 amount per sample, n_{H2} = 1.2 mmol g^{-1}, quasi-elastic broadening was visible already at low temperatures, $T \geq 50$ K, and the integrated area of the quasi-elastic component was larger in comparison to the elastic component, indicating the presence of a considerable amount of mobile adsorbed H_2 (Figure 17c).

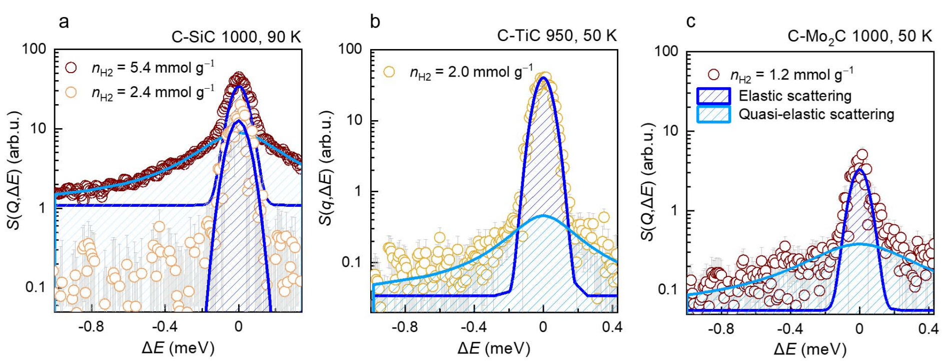

Figure 17. The deconvoluted incoherent dynamic structure factor, $S(q,\Delta E)$ of H_2 at q = 10.7 nm^{-1} in the pores of (a) C-SiC 1000 at 90 K, (b) C-TiC 950 at 50 K and (c) C-Mo_2C 1000 at 50 K.

Although the Hall-Ross jump-diffusion model [91] was suitable to fit the data from C-TiC 950 ja C-SiC 1000, the Singwi-Sjölander jump-diffusion [92] fit was used, since it was suitable for the whole data series of CDC under study. The calculated diffusion coefficients are shown as the Arrhenius-type plot in Figure 18. The calculated temperature-dependant H_2 diffusion coefficients, D_T, of C-Mo_2C 1000 are higher in comparison to the diffusion coefficients of H_2 adsorbed in C-TiC 950 and C-SiC 1000, which demonstrates again that hydrogen mobility in the pores i.e. the porous structure of C-Mo_2C 1000 is less restricted. In the case of lowest H_2 amounts (n_{H2} = 2.4 mmol g^{-1}) in C-SiC 1000, the diffusion coefficients could not be calculated, since no quasi-elastic component was detected, i.e. the H_2 in the pores of C-SiC 1000 was immobile or solid-like. More specifically, at these measurement conditions, the motions of adsorbed H_2 in C-SiC 1000 were too slow to be detected by the limited instrument energy resolution and at these conditions. However, at higher H_2 loading (n_{H2} = 5.4 mmol g^{-1}), the quasi-elastic component became visible and the calculated D_T values are already larger compared to H_2 adsorbed in C-TiC 950 at n_{H2} = 2.0 mmol g^{-1}. This is because when the loading of H_2 in carbon is sufficiently small, only the most favourable adsorption sites are occupied, which result in solid-like adsorbed H_2 in C-SiC 1000 at n_{H2} = 2.4 mmol g^{-1}. Thereafter, when the loading pressure of H_2 is larger (n_{H2} = 5.4 mmol g^{-1}), the remaining H_2 is positioned in the less favourable sites and the self-diffusion coefficient is, thus, larger and the quasi-elastic scattering can be then detected.

The D_T values of hydrogen in the pores of C-TiC 950 at n_{H2} of 2.0 mmol g^{-1} and temperatures up to 70 K was similar to that of liquid H_2 at 20 K [113] (Figure 18). Therefore, H_2 adsorbed in C-TiC 950 demonstrated liquid-like behaviour at low temperatures as well as at low loading pressures.

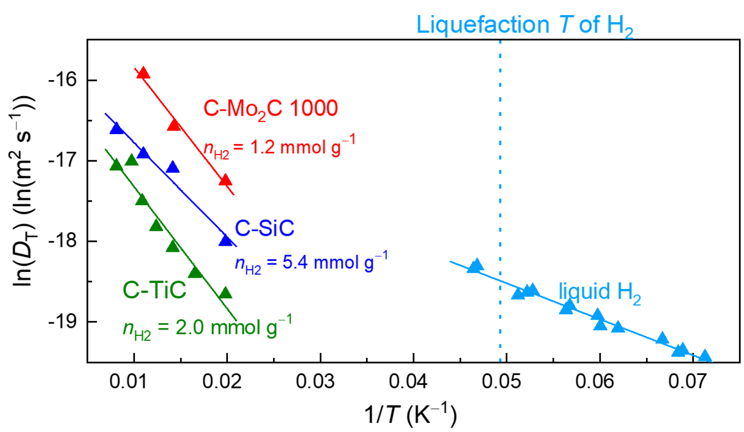

Figure 18. The Arrhenius plot, i.e. the logarithm of self-diffusion coefficient of H_2, $\ln(D_T)$, vs the inverse temperature, $1/T$.

The potential energy landscape in pores with widths in the range 0.6 nm < w < 0.8 nm has been shown to have a strong minima in the middle of the pore, which enhances the strength of the interaction between the adsorbate and the adsorbent [114,115]. Hydrogen is adsorbed in these favourable positions already at very low pressures and when the amount of H_2 per the available pore volume in the carbons sample was small (n_{H2} < 2.4 mmol g^{-1}), most of the H_2 is adsorbed in these minima of the potential energy landscape.

It can be concluded, that the sub-nanometer pores of C-SiC 1000 contribute to the formation of a strongly adsorbed (solid-like) hydrogen layer in the case of n_{H2} = 2.4 mmol g^{-1}. However, in the pores of C-TiC 950, the H_2 was more mobile (according to D_T, H_2 was liquid-like up to 70 K) in case of n_{H2} = 2.0 mmol g^{-1} and the in the pores of C-Mo_2C 1000, the H_2 self-diffusion was the quickest and H_2 was the least confined (Figure 18, Table 12). Thus, the mesoporous structure does not restrict H_2 mobility effectively. Instead, micropores and especially sub-nanometer micropores will help to reduce the repulsive forces between hydrogen molecules and obtain confined H_2 with low diffusion coefficients at milder conditions (i.e. temperature, pressure) compared to pure H_2 at the same conditions.

These results are well explained in terms of the average pore shapes established for these CDC materials. That is, it has been previously determined with SANS, that the prevalent pore shape is spherical in C-SiC 1000, cylindrical in C-TiC 950 and slit-like in C-Mo_2C 1000 [29]. Namely, the pore size distributions of C-SiC 1000 and C-TiC 950 were rather similar (Figure 16a), but H_2 was much more confined in C-SiC 1000 with predominantly spherical pores. This demonstrates the strong effect of pore shape to the confinement of H_2, i.e. the spherical pores are best at confining H_2, while the slit-like pores allow for far more H_2 mobility.

Table 12. Porosity characteristics based on gas adsorption analysis, hydrogen amounts used in QENS experiments and the results about the self-diffusion parameters of H_2 calculated by Arrhenius-type equation.

Carbon	S_{DFT} **m^2 g^{-1}**	V_{tot} **cm^3 g^{-1}**	n_{H2} **mmol g^{-1}**	D_0 **x10^{-7} m^2 s^{-1}**	E_a **kJ mol^{-1}**
C-Mo_2C 1000	820	1.36	1.2	5.1 ± 1.8	1.16 ± 0.17
C-TiC 950	1540	0.68	2.0	1.1 ± 0.3	1.18 ± 0.18
C-SiC 1000	1420	0.51	2.4	-	-
C-SiC 1000			5.4	1.7 ± 0.2	0.96 ± 0.09

S_{DFT} – specific surface area from 2D-NLDFT model, V_{tot} – total volume of pores calculated from the amount of adsorbed gas near the saturation pressure, $p/p°$ = 0.95, $p_{H2,load}$ – the equilibrium pressure of H_2 in the sample holder at 77 K, n_{H2} – the amount of H_2 in the sample cell divided by the mass of the carbon sample, D_0 is the maximal diffusion coefficient and E_a is the activation energy of self-diffusion process of H_2.

6.5. Conclusions

For a large dataset of CDCs synthesized form different precursor carbides, a positive correlation of the T_{syn} and average width of the graphene sheet, L_a, was established with WAXS method. Thus, it was confirmed, that when a higher synthesis temperature is used for the preparation of CDC materials, larger and more defect-free graphene layers are formed. The differences between CDCs with different precursor carbides were also evident. Namely, for most of the CDCs studied, the average stacking size did not increase remarkably with synthesis temperature. However, the CDCs derived from Mo_2C and VC were seen to form larger stacks of graphene layers as the synthesis temperature was increased.

The studied CDCs were classified to different graphitization stages based on their first order Raman spectra. While most of the CDCs were classified to Stage I (i.e. disordered) or Stage II (i.e. nanoparticular), again the carbon materials prepared from Mo_2C and VC at higher temperatures (≥1000 °C) stood out, since these materials could be classified as Stage III (i.e. non-graphitic). This demonstrates the materials C-Mo_2C 1000−1100 and C-VC 1000−1100 showed significant intra graphene layer ordering both in the graphene layer (as evidenced by the first-order Raman spectra) and in the stacking of the graphene layers (as established with WAXS method).

Thereafter, the porous structure of carbons derived for Mo_2C at different synthesis temperatures ranging from 600 to 1000 °C was investigated with small-angle scattering methods. It was demonstrated, that the carbons synthesized at higher temperatures had smoother pores with less angular (i.e. more-slit-like) average shape. Also the decrease in the microporosity with the increase of synthesis temperature was shown with gas adsorption analysis. These results correlate well with the results from the analysis of the Raman spectra and WAXS data on these CDCs. Namely, larger sheets of more ordered graphene layers are formed at higher synthesis temperatures, which result in smoother pore surfaces. Also, the increase in the stacking of graphene layers with the increase in synthesis temperature of C-Mo_2C, explains well the decrease in microporosity. Hence, a great deal of the the microporosity in CDCs lies in between the defected and imperfectly stacked graphene layers. When the stacking of graphene layers becomes more ordered, much of the microporosity is lost.

From the quasi-elastic neutron scattering experiments with CDCs (C-SiC 1000, C-TiC 950 and C-Mo_2C 1000) partly filled with H_2 gas, the impact of the porous structure on the confinement of H_2 was clearly seen. Carbon material C-SiC 1000, which was the least ordered and most microporous carbon of the CDCs studied was best at confining hydrogen. Namely, in the case of very low loading pressure of H_2, the self-diffusion of H_2 was not detected even at 120 K. Carbon material C-TiC 950 has quite similar pore size distribution to C-SiC 1000, but nevertheless was inferior in its capability to confine H_2. This can be explained with the average pore shape, where C-SiC 1000 has been shown to prevalently exhibit spherical and C-TiC 950 prevalently cylindrical pores [29].

C-Mo_2C 1000, which is a mostly mesoporous carbon material and has been established to have quite smooth, mostly slit-like pores, was the worst in confining H_2, even in the case of low temperatures and low H_2 loading pressures. Thus, direct experimental evidence for the strong confinement effect of high curvature, i.e. spherical-like and cylindrical-like, micropores for the successful confinement of H_2 was acquired. These spherical pores might be caused by the curvature in graphene planes, small L_a and little to no ordering in the stacking of graphene layers.

7. SUMMARY

The microstructure of various non-graphitic carbide-derived carbon (CDC) powders was investigated with gas (CO_2, N_2, Ar) sorption analysis, Raman spectroscopy, WAXS and SAXS/SANS methods. In addition, a quasi-elastic neutron scattering (QENS) experiment was conducted to investigate the diffusion of H_2 in the porous structure of three different CDC materials.

From the WAXS data, it was established, that the average graphene platelet size ranged from 2.5 to 8.3 nm, which is bigger than previously thought. In addition, it was demonstrated, that for the most of the CDCs, the stacking size did not increase with the synthesis temperature of the CDC. The exceptions to this rule were CDCs derived from VC and Mo_2C, for which the stacking size increased considerably with the synthesis temperature used in the preparation of these carbon materials..

The methods for the analysis of the Raman spectra of non-graphitic carbons were compared and it was determined, that a deconvolution of the first order Raman spectra with five distribution functions resulted in the most coherent spectral paramaters. It was seen, that the width of the D-band and the parameter $A_{\sum D}/A_{\sum G}$ decreased systematically with the increase of the synthesis temperature of the CDC. These parameters alongside the results from WAXS analysis show that the defect density in the graphene layer will decrease and the size of the graphene layer will increase with the synthesis temperature of the CDC. The average size of the graphene platelet in the CDC calculated on the basis of Raman spectra was bigger on average by 4.4 nm than the size calculated based on WAXS mehod. This discrepancy might indicate the existance of curvature in the CDC materials since the WAXS analysis assumes flat layers, while phonon propagation is not stopped in the case of defected/curved layers of graphene.

Small-angle X-ray and neutron scattering methods were used to investigate the transformation of the porous structure of Mo_2C-derived carbons synthesized at different temperatures ranging form 600 to 1000 °C. Both SANS and SAXS data analysis showed that the surface of the pore becomes smoother as the synthesis temperature of the CDC increases. In addition, it was shown that the average shape of the pores in C-Mo_2C becomes less angular, more slit-like as the synthesis temperature increases up to 1000 °C.

It was demonstrated, that the confinement of H_2 in the pores of carbon materials is highly dependent on the porous structure of the carbon used. When a small amount of H_2 was adsorbed in the carbon derived from SiC at 1000 °C, it was strongly confined and had a practically solid-like structure in the subnanometer pores of this CDC material. The carbon derived from TiC at 950 °C also contained subnanometer pores, but to a lesser extent and this carbon had more pores with widths in the range from 1 to 2 nm. The self-diffusion coefficient of H_2 in the pores of TiC-derived carbon (at temperatures up to 70 K) was seen to be similar to the self-diffusion coefficients of liquid H_2. However, the self-diffusion of H_2 in the mostly mesoporous carbon derived from Mo_2C at 1000 °C was the fastest due to the lack of strongly confining subnanometer pores.

8. REFERENCES

1. Ferrari, A.C.; Robertson, J. Interpretation of Raman Spectra of Disordered and Amorphous Carbon. *Phys. Rev. B Condens. Matter Mater. Phys.* **2000**, *61*, 14095–14107, doi:10.1103/PhysRevB.61.14095.
2. Marsh, H.; Reinoso, F.R. *Activated Carbon*; Elsevier, 2006; ISBN 978-0-08-045596-9.
3. Presser, V.; Heon, M.; Gogotsi, Y. Carbide-Derived Carbons – From Porous Networks to Nanotubes and Graphene. *Advanced Functional Materials* **2011**, *21*, 810–833, doi:10.1002/adfm.201002094.
4. Härmas, R.; Palm, R.; Härmas, M.; Pohl, M.; Kurig, H.; Tallo, I.; Tee, E.; Vaas, I.; Väli, R.; Romann, T.; et al. Influence of Porosity Parameters and Electrolyte Chemical Composition on the Power Densities of Non-Aqueous and Ionic Liquid Based Supercapacitors. *Electrochimica Acta* **2018**, *283*, 931–948, doi:10/gd5nvj.
5. Jäger, R.; Kasatkin, P.E.; Härk, E.; Lust, E. Oxygen Reduction on Molybdenum Carbide Derived Micromesoporous Carbon Electrode in Alkaline Solution. *Electrochemistry Communications* **2013**, *35*, 97–99, doi:10.1016/j.elecom.2013.08.001.
6. Yeon, S.-H.; Jung, K.-N.; Yoon, S.; Shin, K.-H.; Jin, C.-S. Electrochemical Performance of Carbide-Derived Carbon Anodes for Lithium-Ion Batteries. *Journal of Physics and Chemistry of Solids* **2013**, *74*, 1045–1055, doi:10.1016/j.jpcs.2013.02.028.
7. Cui, Z.; Cong, Y.; Du, X.; Li, X.; Zhang, J.; Dong, Z.; Yuan, G.; Li, Y. Silicon Carbide-Derived Carbon Coated Graphitized Mesocarbon Microbead Composites for Anode of Lithium-Ion Battery. *Research & Reviews: Journal of Material Sciences* **2017**, *5*, 16–22, doi:10.4172/2321-6212.1000177.
8. Hassler, J.W. *Activated Carbon*; Chemical Publishing Company, 1963;
9. *IUPAC Compendium of Chemical Terminology: Gold Book*; Nič, M., Jirát, J., Košata, B., Jenkins, A., McNaught, A., Eds.; 2.1.0.; IUPAC: Research Triagle Park, NC, 2009; ISBN 978-0-9678550-9-7.
10. Fitzer, E.; Kochling, K.-H.; Boehm, H.P.; Marsh, H. Recommended terminology for the description of carbon as a solid (IUPAC Recommendations 1995). *Pure and Applied Chemistry* **1995**, *67*, 473–506, doi:10.1351/pac199567030473.
11. Harris, P.J.F. Structure of Non-Graphitising Carbons. *International Materials Reviews* **1997**, *42*, 206–218, doi:10.1179/imr.1997.42.5.206.
12. Stoeckli, H.F. Microporous Carbons and Their Characterization: The Present State of the Art. *Carbon* **1990**, *28*, 1–6, doi:10.1016/0008-6223(90)90086-E.
13. Chae, H.K.; Siberio-Pérez, D.Y.; Kim, J.; Go, Y.; Eddaoudi, M.; Matzger, A.J.; O'Keeffe, M.; Yaghi, O.M. A Route to High Surface Area, Porosity and Inclusion of Large Molecules in Crystals. *Nature* **2004**, *427*, 523–527, doi:10.1038/nature02311.
14. Biscoe, J.; Warren, B.E. An X-Ray Study of Carbon Black. *Journal of Applied Physics* **1942**, *13*, 364–371, doi:10.1063/1.1714879.
15. Oberlin, A. Carbonization and Graphitization. *Carbon* **1984**, *22*, 521–541, doi:10.1016/0008-6223(84)90086-1.
16. Dou, X.; Hasa, I.; Saurel, D.; Vaalma, C.; Wu, L.; Buchholz, D.; Bresser, D.; Komaba, S.; Passerini, S. Hard Carbons for Sodium-Ion Batteries: Structure, Analysis, Sustainability, and Electrochemistry. *Materials Today* **2019**, doi:10.1016/j.mattod.2018.12.040.

17. Franklin, R.E. Crystallite Growth in Graphitizing and Non-Graphitizing Carbons. *Proceedings of the Royal Society of London. Series A, Mathematical and Physical Sciences* **1951**, *209*, 196–218.
18. Heidarinejad, Z.; Dehghani, M.H.; Heidari, M.; Javedan, G.; Ali, I.; Sillanpää, M. Methods for Preparation and Activation of Activated Carbon: A Review. *Environ Chem Lett* **2020**, *18*, 393–415, doi:10.1007/s10311-019-00955-0.
19. Härmas, M.; Thomberg, T.; Kurig, H.; Romann, T.; Jänes, A.; Lust, E. Microporous–Mesoporous Carbons for Energy Storage Synthesized by Activation of Carbonaceous Material by Zinc Chloride, Potassium Hydroxide or Mixture of Them. *Journal of Power Sources* **2016**, *326*, 624–634, doi:10.1016/j.jpowsour.2016.04.038.
20. Härmas, M.; Thomberg, T.; Romann, T.; Jänes, A.; Lust, E. Carbon for Energy Storage Derived from Granulated White Sugar by Hydrothermal Carbonization and Subsequent Zinc Chloride Activation. *J. Electrochem. Soc.* **2017**, *164*, A1866–A1872, doi:10.1149/2.0681709jes.
21. Härmas, M.; Palm, R.; Thomberg, T.; Härmas, R.; Koppel, M.; Paalo, M.; Tallo, I.; Romann, T.; Jänes, A.; Lust, E. Hydrothermal and Peat-Derived Carbons as Electrode Materials for High-Efficient Electrical Double-Layer Capacitors. *J. Appl. Electrochem.* **2020**, *50*, 15–32, doi:10.1007/s10800-019-01364-5.
22. Jänes, A.; Thomberg, T.; Kurig, H.; Lust, E. Nanoscale Fine-Tuning of Porosity of Carbide-Derived Carbon Prepared from Molybdenum Carbide. *Carbon* **2009**, *47*, 23–29, doi:10.1016/j.carbon.2008.07.010.
23. Jänes, A.; Thomberg, T.; Lust, E. Synthesis and Characterisation of Nanoporous Carbide-Derived Carbon by Chlorination of Vanadium Carbide. *Carbon* **2007**, *45*, 2717–2722, doi:10.1016/j.carbon.2007.09.041.
24. Tallo, I.; Thomberg, T.; Kurig, H.; Kontturi, K.; Jänes, A.; Lust, E. Novel Micromesoporous Carbon Materials Synthesized from Tantalum Hafnium Carbide and Tungsten Titanium Carbide. *Carbon* **2014**, *67*, 607–616, doi:10.1016/j.carbon.2013.10.034.
25. Gogotsi, Y.; Nikitin, A.; Ye, H.; Zhou, W.; Fischer, J.E.; Yi, B.; Foley, H.C.; Barsoum, M.W. Nanoporous Carbide-Derived Carbon with Tunable Pore Size. *Nat Mater* **2003**, *2*, 591–594, doi:10.1038/nmat957.
26. Thommes, M.; Kaneko, K.; Neimark, A.V.; Olivier, J.P.; Rodriguez-Reinoso, F.; Rouquerol, J.; Sing, K.S.W. Physisorption of Gases, with Special Reference to the Evaluation of Surface Area and Pore Size Distribution (IUPAC Technical Report). *Pure Appl. Chem.* **2015**, *87*, 1051–1069, doi:10.1515/pac-2014-1117.
27. Jagiello, J.; Kenvin, J.; Celzard, A.; Fierro, V. Enhanced Resolution of Ultra Micropore Size Determination of Biochars and Activated Carbons by Dual Gas Analysis Using N2 and CO2 with 2D-NLDFT Adsorption Models. *Carbon* **2019**, *144*, 206–215, doi:10.1016/j.carbon.2018.12.028.
28. Härk, E.; Ballauff, M. Carbonaceous Materials Investigated by Small-Angle X-Ray and Neutron Scattering. *C* **2020**, *6*, 82, doi:10.3390/c6040082.
29. Kurig, H.; Russina, M.; Tallo, I.; Siebenbürger, M.; Romann, T.; Lust, E. The Suitability of Infinite Slit-Shaped Pore Model to Describe the Pores in Highly Porous Carbon Materials. *Carbon* **2016**, *100*, 617–624, doi:10.1016/j.carbon.2016.01.061.
30. Badaczewski, F.; Loeh, M.O.; Pfaff, T.; Dobrotka, S.; Wallacher, D.; Clemens, D.; Metz, J.; Smarsly, B.M. Peering into the Structural Evolution of Glass-like Carbons Derived from Phenolic Resin by Combining Small-Angle Neutron Scattering with

an Advanced Evaluation Method for Wide-Angle X-Ray Scattering. *Carbon* **2019**, *141*, 169–181, doi:10.1016/j.carbon.2018.09.025.
31. Mileeva, Z.; Ross, D.K.; Wilkinson, D.; King, S.M.; Ryan, T.A.; Sharrock, H. The Use of Small Angle Neutron Scattering with Contrast Matching and Variable Adsorbate Partial Pressures in the Study of Porosity in Activated Carbons. *Carbon* **2012**, *50*, 5062–5075, doi:10.1016/j.carbon.2012.06.046.
32. Dresselhaus, M.S.; Jorio, A.; R.Saito Characterizing Graphene, Graphite, and Carbon Nanotubes by Raman Spectroscopy. *Annual Review of Condensed Matter Physics* **2010**, *1*, 89–108, doi:10.1146/annurev-conmatphys-070909-103919.
33. Telling, M.T.F. *A Practical Guide to Quasi-Elastic Neutron Scattering*; 2020; ISBN 978-1-78801-262-1.
34. Achaw, O.-W. *A Study of the Porosity of Activated Carbons Using the Scanning Electron Microscope*; IntechOpen, 2012; ISBN 978-953-51-0092-8.
35. Rouzaud, J.-N.; Clinard, C. Quantitative High-Resolution Transmission Electron Microscopy: A Promising Tool for Carbon Materials Characterization. *Fuel Processing Technology* **2002**, *77–78*, 229–235, doi:10.1016/S0378-3820(02)00053-X.
36. Ravikovitch, P.I.; Vishnyakov, A.; Russo, R.; Neimark, A.V. Unified Approach to Pore Size Characterization of Microporous Carbonaceous Materials from N2, Ar, and CO2 Adsorption Isotherms†. *Langmuir* **2000**, *16*, 2311–2320, doi:10.1021/la991011c.
37. Jagiello, J.; Betz, W. Characterization of Pore Structure of Carbon Molecular Sieves Using DFT Analysis of Ar and H2 Adsorption Data. *Microporous and Mesoporous Materials* **2008**, *108*, 117–122, doi:10.1016/j.micromeso.2007.03.035.
38. Jagiello, J.; Thommes, M. Comparison of DFT Characterization Methods Based on N2, Ar, CO2, and H2 Adsorption Applied to Carbons with Various Pore Size Distributions. *Carbon* **2004**, *42*, 1227–1232, doi:10.1016/j.carbon.2004.01.022.
39. Jagiello, J. Stable Numerical Solution of the Adsorption Integral Equation Using Splines. *Langmuir* **1994**, *10*, 2778–2785, doi:10.1021/la00020a045.
40. Landers, J.; Gor, G.Y.; Neimark, A.V. Density Functional Theory Methods for Characterization of Porous Materials. *Colloids and Surfaces A: Physicochemical and Engineering Aspects* **2013**, *437*, 3–32, doi:10.1016/j.colsurfa.2013.01.007.
41. Puziy, A.M.; Poddubnaya, O.I.; Gawdzik, B.; Sobiesiak, M. Comparison of Heterogeneous Pore Models QSDFT and 2D-NLDFT and Computer Programs ASiQwin and SAIEUS for Calculation of Pore Size Distribution. *Adsorption* **2016**, *22*, 459–464, doi:10.1007/s10450-015-9704-6.
42. Tuinstra, F.; Koenig, J.L. Raman Spectrum of Graphite. *The Journal of Chemical Physics* **1970**, *53*, 1126–1130, doi:10.1063/1.1674108.
43. Schuepfer, D.B.; Badaczewski, F.; Guerra-Castro, J.M.; Hofmann, D.M.; Heiliger, C.; Smarsly, B.; Klar, P.J. Assessing the Structural Properties of Graphitic and Non-Graphitic Carbons by Raman Spectroscopy. *Carbon* **2020**, *161*, 359–372, doi:10.1016/j.carbon.2019.12.094.
44. Zickler, G.A.; Smarsly, B.; Gierlinger, N.; Peterlik, H.; Paris, O. A Reconsideration of the Relationship between the Crystallite Size La of Carbons Determined by X-Ray Diffraction and Raman Spectroscopy. *Carbon* **2006**, *44*, 3239–3246, doi:10.1016/j.carbon.2006.06.029.
45. Ribeiro-Soares, J.; Oliveros, M.E.; Garin, C.; David, M.V.; Martins, L.G.P.; Almeida, C.A.; Martins-Ferreira, E.H.; Takai, K.; Enoki, T.; Magalhães-Paniago, R.; et al. Structural Analysis of Polycrystalline Graphene Systems by Raman Spectroscopy. *Carbon* **2015**, *95*, 646–652, doi:10.1016/j.carbon.2015.08.020.

46. Sadezky, A.; Muckenhuber, H.; Grothe, H.; Niessner, R.; Pöschl, U. Raman Microspectroscopy of Soot and Related Carbonaceous Materials: Spectral Analysis and Structural Information. *Carbon* **2005**, *43*, 1731–1742, doi:10.1016/j.carbon.2005.02.018.
47. Cuesta, A.; Dhamelincourt, P.; Laureyns, J.; Martínez-Alonso, A.; Tascón, J.M.D. Raman Microprobe Studies on Carbon Materials. *Carbon* **1994**, *32*, 1523–1532, doi:10.1016/0008-6223(94)90148-1.
48. Wang, Y.; Alsmeyer, D.C.; McCreery, R.L. Raman Spectroscopy of Carbon Materials: Structural Basis of Observed Spectra. *Chem. Mater.* **1990**, *2*, 557–563, doi:10.1021/cm00011a018.
49. Mallet-Ladeira, P.; Puech, P.; Weisbecker, P.; Vignoles, G.L.; Monthioux, M. Behavior of Raman D Band for Pyrocarbons with Crystallite Size in the 2–5 Nm Range. *Appl. Phys. A* **2014**, *114*, 759–763, doi:10.1007/s00339-013-7671-x.
50. Negri, F.; Castiglioni, C.; Tommasini, M.; Zerbi, G. A Computational Study of the Raman Spectra of Large Polycyclic Aromatic Hydrocarbons: Toward Molecularly Defined Subunits of Graphite†. *J. Phys. Chem. A* **2002**, *106*, 3306–3317, doi:10.1021/jp0128473.
51. Bragg, W.H.; Bragg, W.L. The Reflection of X-Rays by Crystals. *Proc. R. Soc. Lond. A* **1913**, *88*, 428–438, doi:10.1098/rspa.1913.0040.
52. Faber, K.; Badaczewski, F.; Oschatz, M.; Mondin, G.; Nickel, W.; Kaskel, S.; Smarsly, B.M. In-Depth Investigation of the Carbon Microstructure of Silicon Carbide-Derived Carbons by Wide-Angle X-Ray Scattering. *J. Phys. Chem. C* **2014**, *118*, 15705–15715, doi:10.1021/jp502832x.
53. Härk, E.; Petzold, A.; Goerigk, G.; Ballauff, M.; Kent, B.; Keiderling, U.; Palm, R.; Vaas, I.; Lust, E. The Effect of a Binder on Porosity of the Nanoporous RP-20 Carbon. A Combined Study by Small Angle X-Ray and Neutron Scattering. *Microporous and Mesoporous Materials* **2019**, *275*, 139–146, doi:10.1016/j.micromeso.2018.08.022.
54. Scherrer, P. Bestimmung Der Größe Und Der Inneren Struktur von Kolloidteilchen Mittels Röntgenstrahlen. *Nachrichten von der Gesellschaft der Wissenschaften zu Göttingen, Mathematisch-Physikalische Klasse* **1918**, *1918*, 98–100.
55. Shi, H.; Reimers, J.N.; Dahn, J.R. Structure-Refinement Program for Disordered Carbons. *J Appl Cryst, J Appl Crystallogr* **1993**, *26*, 827–836, doi:10.1107/S0021889893003784.
56. Ruland, W.; Smarsly, B. X-Ray Scattering of Non-Graphitic Carbon: An Improved Method of Evaluation. *J Appl Cryst, J Appl Crystallogr* **2002**, *35*, 624–633, doi:10.1107/S0021889802011007.
57. Azuma, H. A New Structural Model for Nongraphitic Carbons. *J Appl Cryst* **1998**, *31*, 910–916, doi:10.1107/S0021889898008085.
58. Fujimoto, H.; Shiraishi, M. Characterization of Unordered Carbon Using Warren–Bodenstein's Equation. *Carbon* **2001**, *39*, 1753–1761, doi:10.1016/S0008-6223(00)00308-0.
59. Rietveld, H.M. A Profile Refinement Method for Nuclear and Magnetic Structures. *J Appl Cryst* **1969**, *2*, 65–71, doi:10.1107/S0021889869006558.
60. Babu, V.S.; Seehra, M.S. Modeling of Disorder and X-Ray Diffraction in Coal-Based Graphitic Carbons. *Carbon* **1996**, *34*, 1259–1265, doi:10.1016/0008-6223(96)00085-1.

61. Pfaff, T.; Simmermacher, M.; Smarsly, B.M. CarbX : A Program for the Evaluation of Wide-Angle X-Ray Scattering Data of Non-Graphitic Carbons. *J Appl Crystallogr* **2018**, *51*, 219–229, doi:10.1107/S1600576718000195.
62. Pfaff, T.; Badaczewski, F.M.; Loeh, M.O.; Franz, A.; Hoffmann, J.-U.; Reehuis, M.; Zeier, W.G.; Smarsly, B.M. Comparative Microstructural Analysis of Non-graphitic Carbons by Wide-Angle X-Ray and Neutron Scattering. *J. Phys. Chem. C* **2019**, *123*, 20532–20546, doi:10.1021/acs.jpcc.9b03590.
63. Poulain, A.; Dupont, C.; Martinez, P.; Guizani, C.; Drnec, J. Wide-Angle X-Ray Scattering Combined with Pair Distribution Function Analysis of Pyrolyzed Wood. *J Appl Cryst* **2019**, *52*, 60–71, doi:10.1107/S1600576718017685.
64. Schnablegger, H.; Singh, Y. *The SAXS Guide. Getting Acquainted with the Principles*; 4th edition.; Anton Paar GmbH, 2017;
65. Hoinkis, E.; Lima, E.B.F.; Schubert-Bischoff, P. A Study of Carbon Black Corax N330 with Small-Angle Scattering of Neutrons and X-Rays. *Langmuir* **2004**, *20*, 8823–8830, doi:10.1021/la0302596.
66. Jafta, C.J.; Petzold, A.; Risse, S.; Clemens, D.; Wallacher, D.; Goerigk, G.; Ballauff, M. Correlating Pore Size and Shape to Local Disorder in Microporous Carbon: A Combined Small Angle Neutron and X-Ray Scattering Study. *Carbon* **2017**, *123*, 440–447, doi:10.1016/j.carbon.2017.07.046.
67. Mascotto, S.; Kuzmicz, D.; Wallacher, D.; Siebenbürger, M.; Clemens, D.; Risse, S.; Yuan, J.; Antonietti, M.; Ballauff, M. Poly(Ionic Liquid)-Derived Nanoporous Carbon Analyzed by Combination of Gas Physisorption and Small-Angle Neutron Scattering. *Carbon* **2015**, *82*, 425–435, doi:10.1016/j.carbon.2014.10.086.
68. Petzold, A.; Juhl, A.; Scholz, J.; Ufer, B.; Goerigk, G.; Fröba, M.; Ballauff, M.; Mascotto, S. Distribution of Sulfur in Carbon/Sulfur Nanocomposites Analyzed by Small-Angle X-Ray Scattering. *Langmuir* **2016**, *32*, 2780–2786, doi:10.1021/acs.langmuir.5b04734.
69. Smorgonskaya, E.; Kyutt, R.; Shuman, V.A.; Danishevskii, A.M.; Gordeev, S.; Grechinskaya, A. Small-Angle x-Ray Scattering in a Carbon-Sulfur Nanocomposite Produced from Bulk Nanoporous Carbon. *Physics of the Solid State* **2002**, *44*, 2001–2008, doi:10.1134/1.1514795.
70. Hall, P.J.; Brown, S.; Fernandez, J.; Calo, J.M. The Effects of the Electronic Structure of Micropores on the Small Angle Scattering of X-Rays and Neutrons. *Carbon* **2000**, *38*, 1257–1259, doi:10.1016/S0008-6223(00)00096-8.
71. Calo, J.M.; Hall, P.J. The Application of Small Angle Scattering Techniques to Porosity Characterization in Carbons. *Carbon* **2004**, *42*, 1299–1304, doi:10.1016/j.carbon.2004.01.030.
72. *Modern Techniques for Polymer Characterisation*; Pethrick, R.A., Dawkins, J.V., Eds.; J. Wiley: Chichester, West Sussex, England ; New York, 1999; ISBN 978-0-471-96097-3.
73. Perret, R.; Ruland, W. X-Ray Small-Angle Scattering of Non-Graphitizable Carbons. *J Appl Cryst* **1968**, *1*, 308–313, doi:10.1107/S0021889868005558.
74. Ruland, W. Apparent Fractal Dimensions Obtained from Small-Angle Scattering of Carbon Materials. *Carbon* **2001**, *39*, 323–324, doi:10.1016/S0008-6223(00)00256-6.
75. Ruland, W. Small-Angle Scattering of Two-Phase Systems: Determination and Significance of Systematic Deviations from Porod's Law. *J Appl Cryst* **1971**, *4*, 70–73, doi:10.1107/S0021889871006265.
76. *SASView. Http://Www.Sasview.Org/*; 2014;

77. Guinier, A.; Fournet, G. *Small-Angle Scattering of X-Rays*; Wiley, 1955;
78. Feigin, L.A.; Svergun, D.I. *Structure Analysis by Small-Angle X-Ray and Neutron Scattering*; Softcover reprint of the original 1st ed. 1987 edition.; Springer: Place of publication not identified, 2013; ISBN 978-1-4757-6626-4.
79. Laudisio, G.; Dash, R.K.; Singer, J.P.; Yushin, G.; Gogotsi, Y.; Fischer, J.E. Carbide-Derived Carbons: A Comparative Study of Porosity Based on Small-Angle Scattering and Adsorption Isotherms. *Langmuir* **2006**, *22*, 8945–8950, doi:10.1021/la060860e.
80. Hammouda, B. A New Guinier-Porod Model. *Journal of Applied Crystallography* **2010**, *43*, 716–719.
81. Perret, R.; Ruland, W. X-Ray Small-Angle Scattering of Glassy Carbon. *J Appl Cryst* **1972**, *5*, 183–187, doi:10.1107/S0021889872009161.
82. Smarsly, B.; Antonietti, M.; Wolff, T. Evaluation of the Small-Angle x-Ray Scattering of Carbons Using Parametrization Methods. *The Journal of Chemical Physics* **2002**, *116*, 2618–2627, doi:10.1063/1.1433463.
83. Méring, J.; Tchoubar, D. Interprétation de la diffusion centrale des rayons X par les systèmes poreux. I. *J Appl Cryst* **1968**, *1*, 153–165, doi:10.1107/S0021889868005212.
84. Gille, W. Chord Length Distributions and Small-Angle Scattering. *Eur. Phys. J. B* **2000**, *17*, 371–383, doi:10.1007/s100510070116.
85. Stoeckel, D.; Wallacher, D.; Zickler, G.A.; Perlich, J.; Tallarek, U.; Smarsly, B.M. Coherent Analysis of Disordered Mesoporous Adsorbents Using Small Angle X-Ray Scattering and Physisorption Experiments. *Phys. Chem. Chem. Phys.* **2014**, *16*, 6583–6592, doi:10.1039/C3CP55072A.
86. Ciccariello, S. Integral Expressions of the Derivatives of the Small-angle Scattering Correlation Function. *J. Math. Phys.* **1995**, *36*, 219–246, doi:10.1063/1.531303.
87. Ciccariello, S.; Cocco, G.; Benedetti, A.; Enzo, S. Correlation Functions of Amorphous Multiphase Systems. *Phys. Rev. B* **1981**, *23*, 6474–6485, doi:10.1103/PhysRevB.23.6474.
88. Pynn, R. Neutron Scattering – a Primer. *Los Alamos Science* **1990**, *19*, 33.
89. Bée, M. *Quasielastic Neutron Scattering: Principles and Applications in Solid State Chemistry, Biology, and Materials Science*; Adam Hilger: Bristol, England, 1988; ISBN 0-85274-371-8.
90. Chudley, C.T.; Elliott, R.J. Neutron Scattering from a Liquid on a Jump Diffusion Model. *Proc. Phys. Soc.* **1961**, *77*, 353–361, doi:10.1088/0370-1328/77/2/319.
91. Hall, P.L.; Ross, D.K. Incoherent Neutron Scattering Functions for Random Jump Diffusion in Bounded and Infinite Media. *Molecular Physics* **1981**, *42*, 673–682, doi:10.1080/00268978100100521.
92. Singwi, K.S.; Sjölander, A. Diffusive Motions in Water and Cold Neutron Scattering. *Phys. Rev.* **1960**, *119*, 863–871, doi:10.1103/PhysRev.119.863.
93. Jagiello, J.; Olivier, J.P. 2D-NLDFT Adsorption Models for Carbon Slit-Shaped Pores with Surface Energetical Heterogeneity and Geometrical Corrugation. *Carbon* **2013**, *55*, 70–80, doi:10.1016/j.carbon.2012.12.011.
94. Jagiello, J.; Ania, C.; Parra, J.B.; Cook, C. Dual Gas Analysis of Microporous Carbons Using 2D-NLDFT Heterogeneous Surface Model and Combined Adsorption Data of N2 and CO2. *Carbon* **2015**, *91*, 330–337, doi:10.1016/j.carbon.2015.05.004.

95. Tallo, I.; Thomberg, T.; Kontturi, K.; Jänes, A.; Lust, E. Nanostructured Carbide-Derived Carbon Synthesized by Chlorination of Tungsten Carbide. *Carbon* **2011**, *49*, 4427–4433, doi:10.1016/j.carbon.2011.06.033.
96. Tallo, I.; Thomberg, T.; Jänes, A.; Lust, E. Replacing Chlorine with Hydrogen Chloride as a Possible Reactant for Synthesis of Titanium Carbide Derived Carbon Powders for High-Technology Devices. *IOP Conf. Ser.: Mater. Sci. Eng.* **2013**, *49*, 012018, doi:10.1088/1757-899X/49/1/012018.
97. Härmas, R.; Palm, R.; Kurig, H.; Puusepp, L.; Pfaff, T.; Romann, T.; Aruväli, J.; Tallo, I.; Thomberg, T.; Jänes, A.; et al. Carbide-Derived Carbons: WAXS and Raman Spectra for Detailed Structural Analysis. *C* **2021**, *7*, 29, doi:10.3390/c7010029.
98. Härk, E.; Petzold, A.; Goerigk, G.; Risse, S.; Tallo, I.; Härmas, R.; Lust, E.; Ballauff, M. Carbide Derived Carbons Investigated by Small Angle X-Ray Scattering: Inner Surface and Porosity vs. Graphitization. *Carbon* **2019**, *146*, 284–292, doi:10.1016/j.carbon.2019.01.076.
99. Vogtt, K.; Siebenbürger, M.; Clemens, D.; Rabe, C.; Lindner, P.; Russina, M.; Fromme, M.; Mezei, F.; Ballauff, M. A New Time-of-Flight Small-Angle Scattering Instrument at the Helmholtz-Zentrum Berlin: V16/VSANS. *Journal of Applied Crystallography* **2014**, *47*, 237–244, doi:10.1107/S1600576713030227.
100. Palm, R.; Härmas, R.; Härk, E.; Kent, B.; Kurig, H.; Koppel, M.; Russina, M.; Tallo, I.; Romann, T.; Mata, J.; et al. Study of the Structural Curvature in Mo2C Derived Carbons with Contrast Matched Small-Angle Neutron Scattering. *Carbon* **2021**, *171*, 695–703, doi:10.1016/j.carbon.2020.09.070.
101. Kurig, H.; Jänes, A.; Lust, E. Electrochemical Characteristics of Carbide-Derived Carbon|1-Ethyl-3-Methylimidazolium Tetrafluoroborate Supercapacitor Cells. *J. Electrochem. Soc.* **2010**, *157*, A272–A279, doi:10.1149/1.3274208.
102. Käärik, M.; Arulepp, M.; Karelson, M.; Leis, J. The Effect of Graphitization Catalyst on the Structure and Porosity of SiC Derived Carbons. *Carbon* **2008**, *46*, 1579–1587, doi:10.1016/j.carbon.2008.07.003.
103. Mesot, J.; Janssen, S.; Holitzner, L.; Hempelmann, R. Focus: Project of a Space and Time Focussing Time-of-Flight Spectrometer for Cold Neutrons at the Spallation Source SINQ of the Paul Scherrer Institute. *Journal of Neutron Research* **1996**, *3*, 293–310, doi:10.1080/10238169608200202.
104. Do, D.D. *Adsorption Analysis: Equilibria and Kinetics*; Imperial College Press: London, 1998; ISBN 978-1-86094-137-5.
105. Azuah, R.T.; Kneller, L.R.; Qiu, Y.; Tregenna-Piggott, P.L.W.; Brown, C.M.; Copley, J.R.D.; Dimeo, R.M. DAVE: A Comprehensive Software Suite for the Reduction, Visualization, and Analysis of Low Energy Neutron Spectroscopic Data. *J Res Natl Inst Stand Technol* **2009**, *114*, 341–358, doi:10.6028/jres.114.025.
106. Härmas, R.; Palm, R.; Russina, M.; Kurig, H.; Grzimek, V.; Härk, E.; Koppel, M.; Tallo, I.; Paalo, M.; Oll, O.; et al. Transport Properties of H2 Confined in Carbide-Derived Carbons with Different Pore Shapes and Sizes. *Carbon* **2019**, *155*, 122–128, doi:10.1016/j.carbon.2019.08.041.
107. Christians, H.; Brunnengräber, K.; Gläsel, J.; Etzold, Bastian.J.M. Mesoporous and Crystalline Carbide-Derived Carbons: Towards a General Correlation on Synthesis Temperature and Precursor Structure Influence. *Carbon* **2021**, doi:10.1016/j.carbon.2021.01.003.

108. Urbonaite, S.; Hälldahl, L.; Svensson, G. Raman Spectroscopy Studies of Carbide Derived Carbons. *Carbon* **2008**, *46*, 1942–1947, doi:10.1016/j.carbon.2008.08.004.
109. Vázquez-Santos, M.B.; Geissler, E.; László, K.; Rouzaud, J.-N.; Martínez-Alonso, A.; Tascón, J.M.D. Comparative XRD, Raman, and TEM Study on Graphitization of PBO-Derived Carbon Fibers. *J. Phys. Chem. C* **2012**, *116*, 257–268, doi:10.1021/jp2084499.
110. Cançado, L.G.; Silva, M.G. da; Ferreira, E.H.M.; Hof, F.; Kampioti, K.; Huang, K.; Pénicaud, A.; Achete, C.A.; Capaz, R.B.; Jorio, A. Disentangling Contributions of Point and Line Defects in the Raman Spectra of Graphene-Related Materials. *2D Mater.* **2017**, *4*, 025039, doi:10.1088/2053-1583/aa5e77.
111. Tee, E.; Tallo, I.; Kurig, H.; Thomberg, T.; Jänes, A.; Lust, E. Huge Enhancement of Energy Storage Capacity and Power Density of Supercapacitors Based on the Carbon Dioxide Activated Microporous SiC-CDC. *Electrochimica Acta* **2015**, *161*, 364–370, doi:10.1016/j.electacta.2015.02.106.
112. Tallo, I.; Thomberg, T.; Jänes, A.; Lust, E. Comparative Study of Using Chlorine and Hydrogen Chloride for Synthesis of Titanium Carbide Derived Carbon. *ECS Trans.* **2013**, *50*, 3, doi:10.1149/05043.0003ecst.
113. O'Reilly, D.E.; Peterson, E.M. Self-diffusion of Liquid Hydrogen and Deuterium. *J. Chem. Phys.* **1977**, *66*, 934–937, doi:10.1063/1.434001.
114. Liu, J.-C.; Monson, P.A. Does Water Condense in Carbon Pores? *Langmuir* **2005**, *21*, 10219–10225, doi:10.1021/la0508902.
115. Russina, M.; Kemner, E.; Mezei, F. Intra-Cage Dynamics of Molecular Hydrogen Confined in Cages of Two Different Dimensions of Clathrate Hydrates. *Sci Rep* **2016**, *6*, 27417, doi:10.1038/srep27417.

9. SUMMARY IN ESTONIAN

Karbiidist sünteesitud poorsete mittegrafiitsete süsinike struktuuride uurimine ning nende mõju H_2 liikuvusele

Selles töös uuriti erinevate mittegrafiitsete poorsete karbiidist sünteesitud süsinike (CDC) peenstruktuuri. Selleks kasutati gaasisorptsiooni erinevate gaasidega (CO_2, N_2, Ar), Raman spektroskoopiat, laianurgalist röntgenhajumist (WAXS) ning väikesenurgalist neutron- ja röntgenhajumist. Lisaks määrati kvaasielastse neutronhajumise meetodiga (QENS) H_2 liikuvus kolme erineva CDC poorides.

WAXS andmete analüüsi tulemusena selgus, et keskmine grafeenikihi laius oli 2,5 kuni 8,3 nm, mis on suurem, kui varem taoliste süsinikmaterjalide puhul eeldati. Keskmine grafeenikihi laius oli seda suurem, mida suurem oli CDC sünteesitemperatuur. Samas grafeenikihtide virna suurus ei sõltunud enamiku CDC süsinike puhul sünteesitemperatuurist. Ainult molübdeenkarbiidist ja vanaadiumkarbiidist sünteesitud süsinike korral oli näha, kuidas grafeenikihtide virn kasvab sünteesitemperatuuri suurenedes.

CDC süsinike Raman spektrite analüüsiks rakendati ja võrreldi mitmeid eri meetodeid. Selgus et seda tüüpi süsinike I järku Raman spektrite analüüsiks sobib kõige paremini kasutada viie jaotusfunktsiooniga kombinatsiooni. Kui sünteesitemperatuur kasvas, muutus süstemaatiliselt kitsamaks Raman spektri D piik ja vähenes spektrit iseloomustav parameeter $A_{\sum D}/A_{\sum G}$. Koos WAXS analüüsist saadud tulemustega saab sellest järeldada, et defekte jääb grafeenikihis vähemaks ja keskmine grafeenikiht suureneb, kui CDC sünteesitemperatuur kasvab. Raman spektri järgi arvutatud keskmine grafeenikihi suurus oli umbes 4,4 nm suurem võrreldes WAXS analüüsi tulemusena saadud grafeenikihi laiusega. See erinevus viitab sellele, et grafeenikihid CDC materjalides on kaardus, sest WAXS analüüsi eelduseks on lamedad kihid, aga võnkumised, mis põhjustavad Raman hajumist, võivad toimuda ka kaardus grafeenikihtides.

Selleks, et uurida lähemalt molübdeenkarbiidist eri temperatuuridel (600 kuni 1000 °C) sünteesitud süsinike poorset struktuuri, kasutati väikesenurgalist röntgen- ja neutronhajumist. Nähti, et kui sünteesitemperatuur tõuseb, tekib süsinikku rohkem mesopoore, samas kui mikropooride hulk väheneb. Seda toetas ka gaasisorptsiooni analüüs. Väikesenurgahajumise meetodite tulemuste põhjal oli näha, et sünteesitemperatuuri kasvades muutub poorisein süsinikus siledamaks ja poori kuju muutub keskmiselt vähem nurgelisemaks.

Selle, millisel määral on H_2 liikumine kinni peetud teatud poorses süsinikmaterjalis, määrab suuresti süsinikmaterjali poorne struktuur (ehk kui palju ja kui suuri poore see sisaldab). Väike kogus vesinikku, mis oli adsorbeerunud ränikarbiidist sünteesitud süsiniku poorides, oli tugevalt kinnipeetud, sisuliselt liikumatu, ka suhteliselt kõrgel temperatuuril 120 K. Väike kogus vesinikku, mis oli adsorbeerunud titaankarbiidist sünteesitud süsinikul difundeerus ligilähedaselt sama kiirusega kui vedel vesinik, kui temperatuur oli kuni 70 K. Seevastu väike kogus vesinikku, mis oli adsorbeerunud molübdeenkarbiidist sünteesitud süsiniku poorides ei olnud kuigi tugevalt kinnipeetud ja selle difusioon oli üsna kiire ka madalatel temperatuuridel. Selgus, et vesiniku lõksustamisel on oluline alla 1 nm läbimõõduga pooride hulk süsinikus, mis on ränikarbiidist sünteesitud süsinikus suurim. Veel on oluline asjaolu ka poori kuju, sest kuigi 1 nm pooride hulk oli nii räni- kui ka titaankarbiidist sünteesitud süsinikes sarnane, oli ränikarbiidist sünteesitud süsinikus, mille keskmine poori kuju on sfääriline, H_2 tugevamalt lõksustunud.

10. ACKNOWLEDGEMENTS

Firstly, I would like to thank my supervisors prof. Enn Lust, Dr. Heisi Kurig and Dr. Rasmus Palm, who have been immensely patient and supportive. Prof. Lust has been a great example to me with his dedication, hard work and honesty in science. He has encouraged me to work independently and I am sincerely grateful for his trust. Thanks to him I was able to work very flexibly, which was essential when I was juggling family and work responsibilities during the last two years of my PhD studies. I am also very grateful for Dr. Heisi Kurig, my supervisor during MSc studies and the first two years of my PhD studies. She set a great standard to me on how to achieve being a meticulous, yet courageous scientist, who gets work done and who is not afraid of exploring new areas of physical chemistry. She was also a great moral support, always boosting my confidence and lifting my mood with our conversations. Thanks to her, I participated in multiple neutron schools. I owe much gratitude also to Dr. Rasmus Palm, who was my supervisor for the last two and a half years of my PhD studies. He has encouraged me to look beyond my limits and to think outside the box. It is truly inspiring to see how much he can achieve in one work week, how quickly he grasps new theories (and creates his own) and how open he is to new challenges. I aspire to be as effective, courageous and insightful scientist as he is. Only thanks to his help in putting together two of the papers I use in this PhD study, I am able to graduate.

I owe a lot of gratitude also to Dr. Eneli Härk from HZB, who is mainly responsible for the SAXS study on Mo_2C-derived carbons and who let me assist her in a SANS measurement at V4 (data not discussed in this thesis). I am very grateful for the collaboration with her, she has been a great mentor and a role-model. She is a very patient, thorough and understanding person and her experimental skillset is really baffling.

I would like to thank the people, who have conducted the experiments, on which my work is based. First and foremost, Dr. Indrek Tallo, Dr. Maarja Paalo, Dr. Thomas Thomberg and Dr. Alar Jänes for the synthesis of CDC carbon powders. In addition, Dr. Tavo Romann for the measurement of most of the Raman spectra, PhD Jaan Aruväli for the measurement of most of the WAXS patterns, Ms Miriam Koppel, for the measurement of some of the gas adsorption isotherms. A great thanks to Dr. Rasmus Palm, Dr. Heisi Kurig for conducting the SANS experiment with C-Mo_2C at HZB and to Dr. Eneli Härk, Dr Heisi Kurig and Dr. Margarita Russina for conducting the QENS experiment at PSI. I am grateful for the the beam time and support offered by PSI and HZB. Prof. K. Kontturi from the Department of Chemistry at Aalto University, is thanked for the HRTEM images of the carbon samples.

I would also like to thank my office companions at various times, Dr. Ronald Väli, Ms Anu Adamson, Mr Kenneth Tuul and Ms Annabel Olgo for insightful and interesting conversations and for finding time to listen to my occasional ramblings. In addition to my office companions, I would also like to thank Dr.

Ove Korjus, Dr. Pilleriin Peets, Dr. Eliise Tammekivi, Dr. Martin Maide, Mr. Alar Heinsaar, Ms. Miriam Koppel, Mr. Patrick Teppor, Mr. Egert Möller, Ms. Marta-Lisette Pikma, Ms. Laura Puusepp for their companionship in and out of Chemicum. I would like to thank all my colleagues for great company, interesting discussions and good advice. Working alongside with you really has felt like being in a large family.

From the Institute of Chemistry, I would like to thank Dr. Karmen Lust, Dr. Heili Kasuk, Dr. Jaak Nerut and prof. Ivo Leito for giving great lectures and inspiring to achieve excellence in teaching. I admire the patient self-improvement that Dr. Karmen Lust, Dr. Heili Kasuk apply in their lectures despite the numerous hardships they have faced, it is evident that they deeply care about their students. I greatly admire prof. Ivo Leito, for setting a standard on excellent teaching for everybody at the Institute of Chemisty. His ability to explain complicated ideas in a simple, yet fun and captivating way is really amazing. I really enjoyed the challenging lectures by Dr. Jaak Nerut, which were really eye-opening and made me push the limits of my mathematical skills and understanding of electrochemical processes. All in all, it is the most difficult courses, in which I learned the most, that I will also cherish the most.

From the Institute of Chemistry I would also like to thank Ms. Urve Soonets, Ms. Marju Rosenthal, Ms. Säde Viirlaid and Ms. Lilli Paama from the administrative office for your patience in answering my numerous questions. Without your help, the bureaucracy would have been a lot more overwhelming at times.

I would not have achieved anything without the unwavering love and support of my family, especially my husband Meelis, who has been with me throughout thick and thin and continues to support my curiosity and ambitions. I admire how Meelis is seldom worried or anxious, but still gets things done. He has a great ability to quickly diffuse stressful situations with some random lowbrow jokes, I try to replicate him on that. I am grateful of my daughter Kaisa who has brought a lot of happiness, hope and stability to my life. I am also very grateful to those who have helped to babysit her at various times so I could focus on my studies, first and foremost my sister Liisi, Ms. Brita Laht, my mother Aili, and and my father Kustas.

This research was funded by the EU through the European Regional Development Fund under Grants TK141 2014–2020.4.01.15–0011 and TK117 3.2.0101–0030, European Spallation Source under grants SLOKT12026T and SLTKT16432T. In addition, the Graduate School of Functional materials and technologies receiving funding from the European Regional Development Fund in University of Tartu, Estonia. This work for this theis has been also partially supported by Estonian Research Council Institutional Research under Grant IUT20–13 and personal research grants PRG676, PUT55, PUT1033, and PUTJD957.

11. PUBLICATIONS

CURRICULUM VITAE

Name: Riinu Härmas
Date of birth: December 10, 1991
Citizenship: Estonian
Contact: Institute of Chemistry, University of Tartu
Ravila 14a, 50411, Tartu, Estonia
E-mail: riinu.harmas@gmail.com

Education:

2016–… University of Tartu, Institute of Chemistry, PhD student
2014–2016 University of Tartu, Institute of Chemistry, M.Sc *cum laude* (Chemistry)
2011–2014 University of Tartu, Institute of Chemistry, B.Sc *cum laude* (Chemistry)

Professional employment:

2014–… University of Tartu, Institute of Chemistry, Chemist
2017–… AS BIT, editor of chemistry e-textbooks
2014–2016 Ahhaa Science center, Explainer

Scientific publications:

1. R. Palm, **R. Härmas**, E. Härk, B. Kent, H. Kurig, M. Koppel, M. Russina, I. Tallo, T. Romann, J. Mata, K. Tuul, E. Lust, *Study of the structural curvature in Mo2C derived carbons with contrast matched small-angle neutron scattering*. Carbon, 171, **2021**, 695−703.
2. M. Koppel, R. Palm, **R. Härmas**, M. Russina, N. Matsubara, M. Månsson, V. Grzimek, M. Paalo, J. Aruväli, T. Romann, O. Oll, E. Lust, *In Situ Observation of Pressure Modulated Reversible Structural Changes in the Graphitic Domains of Carbide-Derived Carbons*. Carbon, 174, **2021**, 190−200.
3. R. Jäger, P. Teppor, M. Paalo, M. Härmas, A. Adamson, O. Volobujeva, E. Härk, Z. Kochovski, T. Romann, **R. Härmas**, J. Aruväli, A. Kikas, E. Lust, *Synthesis and Characterization of Cobalt and Nitrogen Co-Doped Peat-Derived Carbon Catalysts for Oxygen Reduction in Acidic Media*. Catalysts, 11, **2021**, 715.
4. **R. Harmas**, R. Palm, H. Kurig, L. Puusepp, T. Pfaff, T. Romann, J. Aruvali, I. Tallo, T. Thomberg, A. Janes, E. Lust, *Carbide-Derived Carbons: WAXS and Raman Spectra for Detailed Structural Analysis*. C – Journal of Carbon Research, 7, **2021**, 29.
5. M. Härmas, R. Palm, T. Thomberg, **R. Härmas**, M. Koppel, M. Paalo, I. Tallo, T. Romann, A. Jänes, E. Lust, *Hydrothermal and peat-derived carbons as electrode materials for high-efficient electrical double-layer capacitors*. Journal of Applied Electrochemistry, 50, **2020**, 15−32.

6. C. Ramos, G.-M. Lanno, I. Laidmae, A. Meos, **R. Harmas**, K. Kogermann, *High humidity electrospinning of porous fibers for tuning the release of drug delivery systems*. International Journal of Polymeric Materials, 70, **2020**, 880−892.
7. P. Teppor, R. Jäger, M. Paalo, R. Palm, O. Volobujeva, E. Härk, Z. Kochovski, T. Romann, **R. Härmas**, J. Aruväli, A. Kikas, E. Lust, *Peat-derived carbon-based non-platinum group metal type catalyst for oxygen reduction and evolution reactions*. Electrochemistry Communications, 113, **2020**, 106700.
8. O. Korjus, J. Aruväli, P. Paiste, K. Kooser, S. Granroth, H. Mändar, M. Kodu, **R. Härmas**, M. Maide, M. Ainsar, E. Lust, G. Nurk, *Study of Electrochemical and Crystallographic Changes During Initial Stabilisation of La0.75Sr0.25Cr0.5Mn0.3Ni0.2O3−d Reversible Solid Oxide Cell Electrode*. Fuel Cells, 20 (6), **2020**, 741−752.
9. R. Jäger, P. Teppor, E. Härk, M. Härmas, A. Adamson, M. Paalo, O. Volobujeva, A. Kikas, Z. Kochovski, T. Romann, **R. Härmas**, E. Lust, *Cobalt and Nitrogen Co-Doped Peat Derived Carbon Based Catalysts for Oxygen Reduction*. ECS Transactions, 97 (7), **2020**, 605−613.
10. E. Härk, A. Petzold, G. Goerigk, S. Risse, I. Tallo, **R. Härmas**, E. Lust, M. Ballauff, *Carbide derived carbons investigated by small angle X-ray scattering: Inner surface and porosity vs. graphitization*. Carbon, 146, **2019**, 284−292.
11. **R. Härmas**, R. Palm, M. Russina, H. Kurig, V. Grzimek, E. Härk, M. Koppel, I. Tallo, M. Paalo, O. Oll, J. Embs, E. Lust, *Transport properties of H2 confined in carbide-derived carbons with different pore shapes and sizes*. Carbon, 155, **2019**, 122−128.
12. **R. Härmas**, R. Palm, M. Härmas, M. Pohl, H. Kurig, I. Tallo, E. Tee, I. Vaas, R. Väli, T. Romann, O. Oll, R. Kanarbik, K. Liivand, J. Eskusson, J. Kruusma, T. Thomberg, A. Jänes, P. Miidla, E. Lust, *Influence of porosity parameters and electrolyte chemical composition on the power densities of non-aqueous and ionic liquid based supercapacitors*. Electrochimica Acta, 283, **2018**, 931−948.
13. R. Jäger, P. E. Kasatkin, E. Härk, P. Teppor, T. Romann, **R. Härmas**, I. Tallo, U. Mäeorg, U. Joost, P. Paiste, K. Kirsimäe, E. Lust, *The effect of N precursors in Fe-N/C type catalysts based on activated silicon carbide derived carbon for oxygen reduction activity at various pH values*. Journal of Electroanalytical Chemistry, 823, **2018**, 593−600.

ELULOOKIRJELDUS

Nimi: Riinu Härmas
Sünniaeg: 10. detsember 1991
Kodakondsus: Eesti
Kontakt: Tartu Ülikooli keemia instituut, Ravila 14a, 50411, Tartu, Eesti
E-post: riinu.harmas@gmail.com

Haridus:
2016–… Tartu Ülikool, keemia, doktoriõpe
2014–2016 Tartu Ülikool, keemia, M.Sc *cum laude*
2011–2014 Tartu Ülikool, keemia, B.Sc *cum laude*

Töökogemus:
2014–… Keemik, Tartu Ülikooli keemia instituut
2017–… Keemia toimetaja, AS BIT (Kirjastus Avita)
2014–2016 Giid, Ahhaa teaduskeskus

Teaduspublikatsioonid:
1. R. Palm, **R. Härmas**, E. Härk, B. Kent, H. Kurig, M. Koppel, M. Russina, I. Tallo, T. Romann, J. Mata, K. Tuul, E. Lust, *Study of the structural curvature in Mo2C derived carbons with contrast matched small-angle neutron scattering*. Carbon, 171, **2021**, 695−703.
2. M. Koppel, R. Palm, **R. Härmas**, M. Russina, N. Matsubara, M. Månsson, V. Grzimek, M. Paalo, J. Aruväli, T. Romann, O. Oll, E. Lust, *In Situ Observation of Pressure Modulated Reversible Structural Changes in the Graphitic Domains of Carbide-Derived Carbons*. Carbon, 174, **2021**, 190−200.
3. R. Jäger, P. Teppor, M. Paalo, M. Härmas, A. Adamson, O. Volobujeva, E. Härk, Z. Kochovski, T. Romann, **R. Härmas**, J. Aruväli, A. Kikas, E. Lust, *Synthesis and Characterization of Cobalt and Nitrogen Co-Doped Peat-Derived Carbon Catalysts for Oxygen Reduction in Acidic Media*. Catalysts, 11, **2021**, 715.
4. **R. Harmas**, R. Palm, H. Kurig, L. Puusepp, T. Pfaff, T. Romann, J. Aruvali, I. Tallo, T. Thomberg, A. Janes, E. Lust, *Carbide-Derived Carbons: WAXS and Raman Spectra for Detailed Structural Analysis*. C – Journal of Carbon Research, 7, **2021**, 29.
5. M. Härmas, R. Palm, T. Thomberg, **R. Härmas**, M. Koppel, M. Paalo, I. Tallo, T. Romann, A. Jänes, E. Lust, *Hydrothermal and peat-derived carbons as electrode materials for high-efficient electrical double-layer capacitors*. Journal of Applied Electrochemistry, 50, **2020**, 15−32.
6. C. Ramos, G.-M. Lanno, I. Laidmae, A. Meos, **R. Harmas**, K. Kogermann, *High humidity electrospinning of porous fibers for tuning the*

release of drug delivery systems. International Journal of Polymeric Materials, 70, **2020**, 880−892.

7. P. Teppor, R. Jäger, M. Paalo, R. Palm, O. Volobujeva, E. Härk, Z. Kochovski, T. Romann, **R. Härmas**, J. Aruväli, A. Kikas, E. Lust, *Peat-derived carbon-based non-platinum group metal type catalyst for oxygen reduction and evolution reactions*. Electrochemistry Communications, 113, **2020**, 106700.
8. O. Korjus, J. Aruväli, P. Paiste, K. Kooser, S. Granroth, H. Mändar, M. Kodu, **R. Härmas**, M. Maide, M. Ainsar, E. Lust, G. Nurk, *Study of Electrochemical and Crystallographic Changes During Initial Stabilisation of La0.75Sr0.25Cr0.5Mn0.3Ni0.2O3−d Reversible Solid Oxide Cell Electrode*. Fuel Cells, 20 (6), **2020**, 741−752.
9. R. Jäger, P. Teppor, E. Härk, M. Härmas, A. Adamson, M. Paalo, O. Volobujeva, A. Kikas, Z. Kochovski, T. Romann, **R. Härmas**, E. Lust, *Cobalt and Nitrogen Co-Doped Peat Derived Carbon Based Catalysts for Oxygen Reduction*. ECS Transactions, 97 (7), **2020**, 605−613.
10. E. Härk, A. Petzold, G. Goerigk, S. Risse, I. Tallo, **R. Härmas**, E. Lust, M. Ballauff, *Carbide derived carbons investigated by small angle X-ray scattering: Inner surface and porosity vs. graphitization*. Carbon, 146, **2019**, 284−292.
11. **R. Härmas**, R. Palm, M. Russina, H. Kurig, V. Grzimek, E. Härk, M. Koppel, I. Tallo, M. Paalo, O. Oll, J. Embs, E. Lust, *Transport properties of H2 confined in carbide-derived carbons with different pore shapes and sizes*. Carbon, 155, **2019**, 122−128.
12. **R. Härmas**, R. Palm, M. Härmas, M. Pohl, H. Kurig, I. Tallo, E. Tee, I. Vaas, R. Väli, T. Romann, O. Oll, R. Kanarbik, K. Liivand, J. Eskusson, J. Kruusma, T. Thomberg, A. Jänes, P. Miidla, E. Lust, *Influence of porosity parameters and electrolyte chemical composition on the power densities of non-aqueous and ionic liquid based supercapacitors*. Electrochimica Acta, 283, **2018**, 931−948.
13. R. Jäger, P. E. Kasatkin, E. Härk, P. Teppor, T. Romann, **R. Härmas**, I. Tallo, U. Mäeorg, U. Joost, P. Paiste, K. Kirsimäe, E. Lust, *The effect of N precursors in Fe-N/C type catalysts based on activated silicon carbide derived carbon for oxygen reduction activity at various pH values*. Journal of Electroanalytical Chemistry, 823, **2018**, 593−600.

DISSERTATIONES CHIMICAE UNIVERSITATIS TARTUENSIS

1. **Toomas Tamm.** Quantum-chemical simulation of solvent effects. Tartu, 1993, 110 p.
2. **Peeter Burk.** Theoretical study of gas-phase acid-base equilibria. Tartu, 1994, 96 p.
3. **Victor Lobanov.** Quantitative structure-property relationships in large descriptor spaces. Tartu, 1995, 135 p.
4. **Vahur Mäemets.** The ^{17}O and ^{1}H nuclear magnetic resonance study of H_2O in individual solvents and its charged clusters in aqueous solutions of electrolytes. Tartu, 1997, 140 p.
5. **Andrus Metsala.** Microcanonical rate constant in nonequilibrium distribution of vibrational energy and in restricted intramolecular vibrational energy redistribution on the basis of slater's theory of unimolecular reactions. Tartu, 1997, 150 p.
6. **Uko Maran.** Quantum-mechanical study of potential energy surfaces in different environments. Tartu, 1997, 137 p.
7. **Alar Jänes.** Adsorption of organic compounds on antimony, bismuth and cadmium electrodes. Tartu, 1998, 219 p.
8. **Kaido Tammeveski.** Oxygen electroreduction on thin platinum films and the electrochemical detection of superoxide anion. Tartu, 1998, 139 p.
9. **Ivo Leito.** Studies of Brønsted acid-base equilibria in water and non-aqueous media. Tartu, 1998, 101 p.
10. **Jaan Leis.** Conformational dynamics and equilibria in amides. Tartu, 1998, 131 p.
11. **Toonika Rinken.** The modelling of amperometric biosensors based on oxidoreductases. Tartu, 2000, 108 p.
12. **Dmitri Panov.** Partially solvated Grignard reagents. Tartu, 2000, 64 p.
13. **Kaja Orupõld.** Treatment and analysis of phenolic wastewater with microorganisms. Tartu, 2000, 123 p.
14. **Jüri Ivask.** Ion Chromatographic determination of major anions and cations in polar ice core. Tartu, 2000, 85 p.
15. **Lauri Vares.** Stereoselective Synthesis of Tetrahydrofuran and Tetrahydropyran Derivatives by Use of Asymmetric Horner-Wadsworth-Emmons and Ring Closure Reactions. Tartu, 2000, 184 p.
16. **Martin Lepiku.** Kinetic aspects of dopamine D_2 receptor interactions with specific ligands. Tartu, 2000, 81 p.
17. **Katrin Sak.** Some aspects of ligand specificity of P2Y receptors. Tartu, 2000, 106 p.
18. **Vello Pällin.** The role of solvation in the formation of iotsitch complexes. Tartu, 2001, 95 p.
19. **Katrin Kollist.** Interactions between polycyclic aromatic compounds and humic substances. Tartu, 2001, 93 p.

20. **Ivar Koppel.** Quantum chemical study of acidity of strong and superstrong Brønsted acids. Tartu, 2001, 104 p.
21. **Viljar Pihl.** The study of the substituent and solvent effects on the acidity of OH and CH acids. Tartu, 2001, 132 p.
22. **Natalia Palm.** Specification of the minimum, sufficient and significant set of descriptors for general description of solvent effects. Tartu, 2001, 134 p.
23. **Sulev Sild.** QSPR/QSAR approaches for complex molecular systems. Tartu, 2001, 134 p.
24. **Ruslan Petrukhin.** Industrial applications of the quantitative structure-property relationships. Tartu, 2001, 162 p.
25. **Boris V. Rogovoy.** Synthesis of (benzotriazolyl)carboximidamides and their application in relations with *N*- and *S*-nucleophyles. Tartu, 2002, 84 p.
26. **Koit Herodes.** Solvent effects on UV-vis absorption spectra of some solvatochromic substances in binary solvent mixtures: the preferential solvation model. Tartu, 2002, 102 p.
27. **Anti Perkson.** Synthesis and characterisation of nanostructured carbon. Tartu, 2002, 152 p.
28. **Ivari Kaljurand.** Self-consistent acidity scales of neutral and cationic Brønsted acids in acetonitrile and tetrahydrofuran. Tartu, 2003, 108 p.
29. **Karmen Lust.** Adsorption of anions on bismuth single crystal electrodes. Tartu, 2003, 128 p.
30. **Mare Piirsalu.** Substituent, temperature and solvent effects on the alkaline hydrolysis of substituted phenyl and alkyl esters of benzoic acid. Tartu, 2003, 156 p.
31. **Meeri Sassian.** Reactions of partially solvated Grignard reagents. Tartu, 2003, 78 p.
32. **Tarmo Tamm.** Quantum chemical modelling of polypyrrole. Tartu, 2003. 100 p.
33. **Erik Teinemaa.** The environmental fate of the particulate matter and organic pollutants from an oil shale power plant. Tartu, 2003. 102 p.
34. **Jaana Tammiku-Taul.** Quantum chemical study of the properties of Grignard reagents. Tartu, 2003. 120 p.
35. **Andre Lomaka.** Biomedical applications of predictive computational chemistry. Tartu, 2003. 132 p.
36. **Kostyantyn Kirichenko.** Benzotriazole – Mediated Carbon–Carbon Bond Formation. Tartu, 2003. 132 p.
37. **Gunnar Nurk.** Adsorption kinetics of some organic compounds on bismuth single crystal electrodes. Tartu, 2003, 170 p.
38. **Mati Arulepp.** Electrochemical characteristics of porous carbon materials and electrical double layer capacitors. Tartu, 2003, 196 p.
39. **Dan Cornel Fara.** QSPR modeling of complexation and distribution of organic compounds. Tartu, 2004, 126 p.
40. **Riina Mahlapuu.** Signalling of galanin and amyloid precursor protein through adenylate cyclase. Tartu, 2004, 124 p.

41. **Mihkel Kerikmäe.** Some luminescent materials for dosimetric applications and physical research. Tartu, 2004, 143 p.
42. **Jaanus Kruusma.** Determination of some important trace metal ions in human blood. Tartu, 2004, 115 p.
43. **Urmas Johanson.** Investigations of the electrochemical properties of polypyrrole modified electrodes. Tartu, 2004, 91 p.
44. **Kaido Sillar.** Computational study of the acid sites in zeolite ZSM-5. Tartu, 2004, 80 p.
45. **Aldo Oras.** Kinetic aspects of dATPαS interaction with $P2Y_1$ receptor. Tartu, 2004, 75 p.
46. **Erik Mölder.** Measurement of the oxygen mass transfer through the air-water interface. Tartu, 2005, 73 p.
47. **Thomas Thomberg.** The kinetics of electroreduction of peroxodisulfate anion on cadmium (0001) single crystal electrode. Tartu, 2005, 95 p.
48. **Olavi Loog.** Aspects of condensations of carbonyl compounds and their imine analogues. Tartu, 2005, 83 p.
49. **Siim Salmar.** Effect of ultrasound on ester hydrolysis in aqueous ethanol. Tartu, 2006, 73 p.
50. **Ain Uustare.** Modulation of signal transduction of heptahelical receptors by other receptors and G proteins. Tartu, 2006, 121 p.
51. **Sergei Yurchenko.** Determination of some carcinogenic contaminants in food. Tartu, 2006, 143 p.
52. **Kaido Tämm.** QSPR modeling of some properties of organic compounds. Tartu, 2006, 67 p.
53. **Olga Tšubrik.** New methods in the synthesis of multisubstituted hydrazines. Tartu. 2006, 183 p.
54. **Lilli Sooväli.** Spectrophotometric measurements and their uncertainty in chemical analysis and dissociation constant measurements. Tartu, 2006, 125 p.
55. **Eve Koort.** Uncertainty estimation of potentiometrically measured ph and pK_a values. Tartu, 2006, 139 p.
56. **Sergei Kopanchuk.** Regulation of ligand binding to melanocortin receptor subtypes. Tartu, 2006, 119 p.
57. **Silvar Kallip.** Surface structure of some bismuth and antimony single crystal electrodes. Tartu, 2006, 107 p.
58. **Kristjan Saal.** Surface silanization and its application in biomolecule coupling. Tartu, 2006, 77 p.
59. **Tanel Tätte.** High viscosity $Sn(OBu)_4$ oligomeric concentrates and their applications in technology. Tartu, 2006, 91 p.
60. **Dimitar Atanasov Dobchev**. Robust QSAR methods for the prediction of properties from molecular structure. Tartu, 2006, 118 p.
61. **Hannes Hagu**. Impact of ultrasound on hydrophobic interactions in solutions. Tartu, 2007, 81 p.
62. **Rutha Jäger.** Electroreduction of peroxodisulfate anion on bismuth electrodes. Tartu, 2007, 142 p.

63. **Kaido Viht.** Immobilizable bisubstrate-analogue inhibitors of basophilic protein kinases: development and application in biosensors. Tartu, 2007, 88 p.
64. **Eva-Ingrid Rõõm.** Acid-base equilibria in nonpolar media. Tartu, 2007, 156 p.
65. **Sven Tamp.** DFT study of the cesium cation containing complexes relevant to the cesium cation binding by the humic acids. Tartu, 2007, 102 p.
66. **Jaak Nerut.** Electroreduction of hexacyanoferrate(III) anion on Cadmium (0001) single crystal electrode. Tartu, 2007, 180 p.
67. **Lauri Jalukse.** Measurement uncertainty estimation in amperometric dissolved oxygen concentration measurement. Tartu, 2007, 112 p.
68. **Aime Lust.** Charge state of dopants and ordered clusters formation in CaF_2:Mn and CaF_2:Eu luminophors. Tartu, 2007, 100 p.
69. **Iiris Kahn**. Quantitative Structure-Activity Relationships of environmentally relevant properties. Tartu, 2007, 98 p.
70. **Mari Reinik.** Nitrates, nitrites, N-nitrosamines and polycyclic aromatic hydrocarbons in food: analytical methods, occurrence and dietary intake. Tartu, 2007, 172 p.
71. **Heili Kasuk.** Thermodynamic parameters and adsorption kinetics of organic compounds forming the compact adsorption layer at Bi single crystal electrodes. Tartu, 2007, 212 p.
72. **Erki Enkvist.** Synthesis of adenosine-peptide conjugates for biological applications. Tartu, 2007, 114 p.
73. **Svetoslav Hristov Slavov**. Biomedical applications of the QSAR approach. Tartu, 2007, 146 p.
74. **Eneli Härk.** Electroreduction of complex cations on electrochemically polished Bi(*hkl*) single crystal electrodes. Tartu, 2008, 158 p.
75. **Priit Möller.** Electrochemical characteristics of some cathodes for medium temperature solid oxide fuel cells, synthesized by solid state reaction technique. Tartu, 2008, 90 p.
76. **Signe Viggor.** Impact of biochemical parameters of genetically different pseudomonads at the degradation of phenolic compounds. Tartu, 2008, 122 p.
77. **Ave Sarapuu.** Electrochemical reduction of oxygen on quinone-modified carbon electrodes and on thin films of platinum and gold. Tartu, 2008, 134 p.
78. **Agnes Kütt.** Studies of acid-base equilibria in non-aqueous media. Tartu, 2008, 198 p.
79. **Rouvim Kadis.** Evaluation of measurement uncertainty in analytical chemistry: related concepts and some points of misinterpretation. Tartu, 2008, 118 p.
80. **Valter Reedo.** Elaboration of IVB group metal oxide structures and their possible applications. Tartu, 2008, 98 p.
81. **Aleksei Kuznetsov.** Allosteric effects in reactions catalyzed by the cAMP-dependent protein kinase catalytic subunit. Tartu, 2009, 133 p.

82. **Aleksei Bredihhin.** Use of mono- and polyanions in the synthesis of multisubstituted hydrazine derivatives. Tartu, 2009, 105 p.
83. **Anu Ploom.** Quantitative structure-reactivity analysis in organosilicon chemistry. Tartu, 2009, 99 p.
84. **Argo Vonk.** Determination of adenosine A_{2A}- and dopamine D_1 receptor-specific modulation of adenylate cyclase activity in rat striatum. Tartu, 2009, 129 p.
85. **Indrek Kivi.** Synthesis and electrochemical characterization of porous cathode materials for intermediate temperature solid oxide fuel cells. Tartu, 2009, 177 p.
86. **Jaanus Eskusson.** Synthesis and characterisation of diamond-like carbon thin films prepared by pulsed laser deposition method. Tartu, 2009, 117 p.
87. **Marko Lätt.** Carbide derived microporous carbon and electrical double layer capacitors. Tartu, 2009, 107 p.
88. **Vladimir Stepanov.** Slow conformational changes in dopamine transporter interaction with its ligands. Tartu, 2009, 103 p.
89. **Aleksander Trummal.** Computational Study of Structural and Solvent Effects on Acidities of Some Brønsted Acids. Tartu, 2009, 103 p.
90. **Eerold Vellemäe.** Applications of mischmetal in organic synthesis. Tartu, 2009, 93 p.
91. **Sven Parkel.** Ligand binding to 5-HT_{1A} receptors and its regulation by Mg^{2+} and Mn^{2+}. Tartu, 2010, 99 p.
92. **Signe Vahur.** Expanding the possibilities of ATR-FT-IR spectroscopy in determination of inorganic pigments. Tartu, 2010, 184 p.
93. **Tavo Romann**. Preparation and surface modification of bismuth thin film, porous, and microelectrodes. Tartu, 2010, 155 p.
94. **Nadežda Aleksejeva.** Electrocatalytic reduction of oxygen on carbon nanotube-based nanocomposite materials. Tartu, 2010, 147 p.
95. **Marko Kullapere.** Electrochemical properties of glassy carbon, nickel and gold electrodes modified with aryl groups. Tartu, 2010, 233 p.
96. **Liis Siinor.** Adsorption kinetics of ions at Bi single crystal planes from aqueous electrolyte solutions and room-temperature ionic liquids. Tartu, 2010, 101 p.
97. **Angela Vaasa.** Development of fluorescence-based kinetic and binding assays for characterization of protein kinases and their inhibitors. Tartu 2010, 101 p.
98. **Indrek Tulp.** Multivariate analysis of chemical and biological properties. Tartu 2010, 105 p.
99. **Aare Selberg.** Evaluation of environmental quality in Northern Estonia by the analysis of leachate. Tartu 2010, 117 p.
100. **Darja Lavõgina.** Development of protein kinase inhibitors based on adenosine analogue-oligoarginine conjugates. Tartu 2010, 248 p.
101. **Laura Herm.** Biochemistry of dopamine D_2 receptors and its association with motivated behaviour. Tartu 2010, 156 p.

102. **Terje Raudsepp.** Influence of dopant anions on the electrochemical properties of polypyrrole films. Tartu 2010, 112 p.
103. **Margus Marandi.** Electroformation of Polypyrrole Films: *In-situ* AFM and STM Study. Tartu 2011, 116 p.
104. **Kairi Kivirand.** Diamine oxidase-based biosensors: construction and working principles. Tartu, 2011, 140 p.
105. **Anneli Kruve.** Matrix effects in liquid-chromatography electrospray mass-spectrometry. Tartu, 2011, 156 p.
106. **Gary Urb.** Assessment of environmental impact of oil shale fly ash from PF and CFB combustion. Tartu, 2011, 108 p.
107. **Nikita Oskolkov.** A novel strategy for peptide-mediated cellular delivery and induction of endosomal escape. Tartu, 2011, 106 p.
108. **Dana Martin.** The QSPR/QSAR approach for the prediction of properties of fullerene derivatives. Tartu, 2011, 98 p.
109. **Säde Viirlaid.** Novel glutathione analogues and their antioxidant activity. Tartu, 2011, 106 p.
110. **Ülis Sõukand.** Simultaneous adsorption of Cd^{2+}, Ni^{2+}, and Pb^{2+} on peat. Tartu, 2011, 124 p.
111. **Lauri Lipping.** The acidity of strong and superstrong Brønsted acids, an outreach for the "limits of growth": a quantum chemical study. Tartu, 2011, 124 p.
112. **Heisi Kurig.** Electrical double-layer capacitors based on ionic liquids as electrolytes. Tartu, 2011, 146 p.
113. **Marje Kasari.** Bisubstrate luminescent probes, optical sensors and affinity adsorbents for measurement of active protein kinases in biological samples. Tartu, 2012, 126 p.
114. **Kalev Takkis.** Virtual screening of chemical databases for bioactive molecules. Tartu, 2012, 122 p.
115. **Ksenija Kisseljova**. Synthesis of aza-β^3-amino acid containing peptides and kinetic study of their phosphorylation by protein kinase A. Tartu, 2012, 104 p.
116. **Riin Rebane.** Advanced method development strategy for derivatization LC/ESI/MS. Tartu, 2012, 184 p.
117. **Vladislav Ivaništšev.** Double layer structure and adsorption kinetics of ions at metal electrodes in room temperature ionic liquids. Tartu, 2012, 128 p.
118. **Irja Helm.** High accuracy gravimetric Winkler method for determination of dissolved oxygen. Tartu, 2012, 139 p.
119. **Karin Kipper.** Fluoroalcohols as Components of LC-ESI-MS Eluents: Usage and Applications. Tartu, 2012, 164 p.
120. **Arno Ratas.** Energy storage and transfer in dosimetric luminescent materials. Tartu, 2012, 163 p.
121. **Reet Reinart-Okugbeni**. Assay systems for characterisation of subtype-selective binding and functional activity of ligands on dopamine receptors. Tartu, 2012, 159 p.

122. **Lauri Sikk.** Computational study of the Sonogashira cross-coupling reaction. Tartu, 2012, 81 p.
123. **Karita Raudkivi.** Neurochemical studies on inter-individual differences in affect-related behaviour of the laboratory rat. Tartu, 2012, 161 p.
124. **Indrek Saar.** Design of GalR2 subtype specific ligands: their role in depression-like behavior and feeding regulation. Tartu, 2013, 126 p.
125. **Ann Laheäär.** Electrochemical characterization of alkali metal salt based non-aqueous electrolytes for supercapacitors. Tartu, 2013, 127 p.
126. **Kerli Tõnurist.** Influence of electrospun separator materials properties on electrochemical performance of electrical double-layer capacitors. Tartu, 2013, 147 p.
127. **Kaija Põhako-Esko.** Novel organic and inorganic ionogels: preparation and characterization. Tartu, 2013, 124 p.
128. **Ivar Kruusenberg.** Electroreduction of oxygen on carbon nanomaterial-based catalysts. Tartu, 2013, 191 p.
129. **Sander Piiskop.** Kinetic effects of ultrasound in aqueous acetonitrile solutions. Tartu, 2013, 95 p.
130. **Ilona Faustova**. Regulatory role of L-type pyruvate kinase N-terminal domain. Tartu, 2013, 109 p.
131. **Kadi Tamm.** Synthesis and characterization of the micro-mesoporous anode materials and testing of the medium temperature solid oxide fuel cell single cells. Tartu, 2013, 138 p.
132. **Iva Bozhidarova Stoyanova-Slavova.** Validation of QSAR/QSPR for regulatory purposes. Tartu, 2013, 109 p.
133. **Vitali Grozovski**. Adsorption of organic molecules at single crystal electrodes studied by *in situ* STM method. Tartu, 2014, 146 p.
134. **Santa Veikšina**. Development of assay systems for characterisation of ligand binding properties to melanocortin 4 receptors. Tartu, 2014, 151 p.
135. **Jüri Liiv.** PVDF (polyvinylidene difluoride) as material for active element of twisting-ball displays. Tartu, 2014, 111 p.
136. **Kersti Vaarmets.** Electrochemical and physical characterization of pristine and activated molybdenum carbide-derived carbon electrodes for the oxygen electroreduction reaction. Tartu, 2014, 131 p.
137. **Lauri Tõntson**. Regulation of G-protein subtypes by receptors, guanine nucleotides and Mn^{2+}. Tartu, 2014, 105 p.
138. **Aiko Adamson.** Properties of amine-boranes and phosphorus analogues in the gas phase. Tartu, 2014, 78 p.
139. **Elo Kibena**. Electrochemical grafting of glassy carbon, gold, highly oriented pyrolytic graphite and chemical vapour deposition-grown graphene electrodes by diazonium reduction method. Tartu, 2014, 184 p.
140. **Teemu Näykki.** Novel Tools for Water Quality Monitoring – From Field to Laboratory. Tartu, 2014, 202 p.
141. **Karl Kaupmees.** Acidity and basicity in non-aqueous media: importance of solvent properties and purity. Tartu, 2014, 128 p.

142. **Oleg Lebedev**. Hydrazine polyanions: different strategies in the synthesis of heterocycles. Tartu, 2015, 118 p.
143. **Geven Piir.** Environmental risk assessment of chemicals using QSAR methods. Tartu, 2015, 123 p.
144. **Olga Mazina.** Development and application of the biosensor assay for measurements of cyclic adenosine monophosphate in studies of G protein-coupled receptor signalinga. Tartu, 2015, 116 p.
145. **Sandip Ashokrao Kadam.** Anion receptors: synthesis and accurate binding measurements. Tartu, 2015, 116 p.
146. **Indrek Tallo.** Synthesis and characterization of new micro-mesoporous carbide derived carbon materials for high energy and power density electrical double layer capacitors. Tartu, 2015, 148 p.
147. **Heiki Erikson.** Electrochemical reduction of oxygen on nanostructured palladium and gold catalysts. Tartu, 2015, 204 p.
148. **Erik Anderson.** *In situ* Scanning Tunnelling Microscopy studies of the interfacial structure between Bi(111) electrode and a room temperature ionic liquid. Tartu, 2015, 118 p.
149. **Girinath G. Pillai.** Computational Modelling of Diverse Chemical, Biochemical and Biomedical Properties. Tartu, 2015, 140 p.
150. **Piret Pikma.** Interfacial structure and adsorption of organic compounds at Cd(0001) and Sb(111) electrodes from ionic liquid and aqueous electrolytes: an *in situ* STM study. Tartu, 2015, 126 p.
151. **Ganesh babu Manoharan.** Combining chemical and genetic approaches for photoluminescence assays of protein kinases. Tartu, 2016, 126 p.
152. **Carolin Siimenson**. Electrochemical characterization of halide ion adsorption from liquid mixtures at Bi(111) and pyrolytic graphite electrode surface. Tartu, 2016, 110 p.
153. **Asko Laaniste.** Comparison and optimisation of novel mass spectrometry ionisation sources. Tartu, 2016, 156 p.
154. **Hanno Evard.** Estimating limit of detection for mass spectrometric analysis methods. Tartu, 2016, 224 p.
155. **Kadri Ligi.** Characterization and application of protein kinase-responsive organic probes with triplet-singlet energy transfer. Tartu, 2016, 122 p.
156. **Margarita Kagan.** Biosensing penicillins' residues in milk flows. Tartu, 2016, 130 p.
157. **Marie Kriisa.** Development of protein kinase-responsive photoluminescent probes and cellular regulators of protein phosphorylation. Tartu, 2016, 106 p.
158. **Mihkel Vestli.** Ultrasonic spray pyrolysis deposited electrolyte layers for intermediate temperature solid oxide fuel cells. Tartu, 2016, 156 p.
159. **Silver Sepp**. Influence of porosity of the carbide-derived carbon on the properties of the composite electrocatalysts and characteristics of polymer electrolyte fuel cells. Tartu, 2016, 137 p.
160. **Kristjan Haav**. Quantitative relative equilibrium constant measurements in supramolecular chemistry. Tartu, 2017, 158 p.

161. **Anu Teearu**. Development of MALDI-FT-ICR-MS methodology for the analysis of resinous materials. Tartu, 2017, 205 p.
162. **Taavi Ivan**. Bifunctional inhibitors and photoluminescent probes for studies on protein complexes. Tartu, 2017, 140 p.
163. **Maarja-Liisa Oldekop**. Characterization of amino acid derivatization reagents for LC-MS analysis. Tartu, 2017, 147 p.
164. **Kristel Jukk**. Electrochemical reduction of oxygen on platinum- and palladium-based nanocatalysts. Tartu, 2017, 250 p.
165. **Siim Kukk**. Kinetic aspects of interaction between dopamine transporter and *N*-substituted nortropane derivatives. Tartu, 2017, 107 p.
166. **Birgit Viira**. Design and modelling in early drug development in targeting HIV-1 reverse transcriptase and Malaria. Tartu, 2017, 172 p.
167. **Rait Kivi**. Allostery in cAMP dependent protein kinase catalytic subunit. Tartu, 2017, 115 p.
168. **Agnes Heering**. Experimental realization and applications of the unified acidity scale. Tartu, 2017, 123 p.
169. **Delia Juronen**. Biosensing system for the rapid multiplex detection of mastitis-causing pathogens in milk. Tartu, 2018, 85 p.
170. **Hedi Rahnel.** ARC-inhibitors: from reliable biochemical assays to regulators of physiology of cells. Tartu, 2018, 176 p.
171. **Anton Ruzanov.** Computational investigation of the electrical double layer at metal–aqueous solution and metal–ionic liquid interfaces. Tartu, 2018, 129 p.
172. **Katrin Kestav.** Crystal Structure-Guided Development of Bisubstrate-Analogue Inhibitors of Mitotic Protein Kinase Haspin. Tartu, 2018, 166 p.
173. **Mihkel Ilisson.** Synthesis of novel heterocyclic hydrazine derivatives and their conjugates. Tartu, 2018, 101 p.
174. **Anni Allikalt.** Development of assay systems for studying ligand binding to dopamine receptors. Tartu, 2018, 160 p.
175. **Ove Oll.** Electrical double layer structure and energy storage characteristics of ionic liquid based capacitors. Tartu, 2018, 187 p.
176. **Rasmus Palm.** Carbon materials for energy storage applications. Tartu, 2018, 114 p.
177. **Jörgen Metsik.** Preparation and stability of poly(3,4-ethylenedioxythiophene) thin films for transparent electrode applications. Tartu, 2018, 111 p.
178. **Sofja Tšepelevitš.** Experimental studies and modeling of solute-solvent interactions. Tartu, 2018, 109 p.
179. **Märt Lõkov.** Basicity of some nitrogen, phosphorus and carbon bases in acetonitrile. Tartu, 2018, 104 p.
180. **Anton Mastitski**. Preparation of α-aza-amino acid precursors and related compounds by novel methods of reductive one-pot alkylation and direct alkylation. Tartu, 2018, 155 p.
181. **Jürgen Vahter**. Development of bisubstrate inhibitors for protein kinase CK2. Tartu, 2019, 186 p.

182. **Piia Liigand.** Expanding and improving methodology and applications of ionization efficiency measurements. Tartu, 2019, 189 p.
183. **Sigrid Selberg.** Synthesis and properties of lipophilic phosphazene-based indicator molecules. Tartu, 2019, 74 p.
184. **Jaanus Liigand.** Standard substance free quantification for LC/ESI/MS analysis based on the predicted ionization efficiencies. Tartu, 2019, 254 p.
185. **Marek Mooste.** Surface and electrochemical characterisation of aryl film and nanocomposite material modified carbon and metal-based electrodes. Tartu, 2019, 304 p.
186. **Mare Oja.** Experimental investigation and modelling of pH profiles for effective membrane permeability of drug substances. Tartu, 2019, 306 p.
187. **Sajid Hussain.** Electrochemical reduction of oxygen on supported Pt catalysts. Tartu, 2019, 220 p.
188. **Ronald Väli.** Glucose-derived hard carbon electrode materials for sodium-ion batteries. Tartu, 2019, 180 p.
189. **Ester Tee.** Analysis and development of selective synthesis methods of hierarchical micro- and mesoporous carbons. Tartu, 2019, 210 p.
190. **Martin Maide.** Influence of the microstructure and chemical composition of the fuel electrode on the electrochemical performance of reversible solid oxide fuel cell. Tartu, 2020, 144 p.
191. **Edith Viirlaid.** Biosensing Pesticides in Water Samples. Tartu, 2020, 102 p.
192. **Maike Käärik.** Nanoporous carbon: the controlled nanostructure, and structure-property relationships. Tartu, 2020, 162 p.
193. **Artur Gornischeff.** Study of ionization efficiencies for derivatized compounds in LC/ESI/MS and their application for targeted analysis. Tartu, 2020, 124 p.
194. **Reet Link.** Ligand binding, allosteric modulation and constitutive activity of melanocortin-4 receptors. Tartu, 2020, 108 p.
195. **Pilleriin Peets.** Development of instrumental methods for the analysis of textile fibres and dyes. Tartu, 2020, 150 p.
196. **Larisa Ivanova.** Design of active compounds against neurodegenerative diseases. Tartu, 2020, 152 p.
197. **Meelis Härmas.** Impact of activated carbon microstructure and porosity on electrochemical performance of electrical double-layer capacitors. Tartu, 2020, 122 p.
198. **Ruta Hecht.** Novel Eluent Additives for LC-MS Based Bioanalytical Methods. Tartu, 2020, 202 p.
199. **Max Hecht.** Advances in the Development of a Point-of-Care Mass Spectrometer Test. Tartu, 2020, 168 p.
200. **Ida Rahu.** Bromine formation in inorganic bromide/nitrate mixtures and its application for oxidative aromatic bromination. Tartu, 2020, 116 p.
201. **Sander Ratso**. Electrocatalysis of oxygen reduction on non-precious metal catalysts. Tartu, 2020, 371 p.
202. **Astrid Darnell.** Computational design of anion receptors and evaluation of host-guest binding. Tartu, 2021, 150 p.

203. **Ove Korjus.** The development of ceramic fuel electrode for solid oxide cells. Tartu, 2021, 150 p.
204. **Merit Oss.** Ionization efficiency in electrospray ionization source and its relations to compounds' physico-chemical properties. Tartu, 2021, 124 p.
205. **Madis Lüsi**. Electroreduction of oxygen on nanostructured palladium catalysts. Tartu, 2021, 180 p.
206. **Eliise Tammekivi.** Derivatization and quantitative gas-chromatographic analysis of oils. Tartu, 2021, 122 p.
207. **Simona Selberg.** Development of Small-Molecule Regulators of Epitranscriptomic Processes. Tartu, 2021, 122 p.
208. **Olivier Etebe Nonga.** Inhibitors and photoluminescent probes for in vitro studies on protein kinases PKA and PIM. Tartu, 2021, 189 p.